

Dynamic Crack Growth Normal to an Interface in Bi-Layered Materials: An Experimental Study Using Digital Gradient Sensing Technique

B.M. Sundaram¹ · H.V. Tippur¹

Received: 4 October 2014 / Accepted: 13 April 2015 / Published online: 16 May 2015
© Society for Experimental Mechanics 2015

Abstract The dynamic fracture behavior of layered architectures is experimentally studied. Specifically, crack penetration, trapping, and branching at an interface are examined. A newly introduced optical technique called Digital Gradient Sensing (DGS) that quantifies elasto-optic effects due to a non-uniform state of stress is extended to perform full-field measurements during the fracture event using ultrahigh-speed photography. By exploiting the richness of two simultaneously measured orthogonal stress gradient fields, a modified approach for extracting stress intensity factors (SIFs) is implemented for propagating crack-tips under mixed-mode conditions. The method is first calibrated using a quasi-static experiment complemented by finite element simulations before implementing it for studying dynamic mixed-mode fracture mechanics of layered configurations. The layered systems considered consist of two PMMA sheets bonded using an acrylic adhesive with the interface oriented normally to the initial crack propagation direction. Interfaces are characterized as ‘strong’ and ‘weak’ by their crack initiation toughness. The dynamic fracture of monolithic PMMA sheet is also studied in the same configuration for comparison. The crack growth and fracture parameter histories of propagating cracks are evaluated. The interface is shown to drastically perturb crack growth behavior resulting in higher dissipation of fracture energy by exciting crack trapping, branching, and mixed-mode growth mechanisms.

Keywords Optical metrology · Digital gradient sensing · Transparent material · Interfaces · Dynamic fracture · Mixed-mode fracture

Introduction

Transparent materials are used in various aerospace, automotive, and military applications as windshields, protective canopies, face-shields, etc. In such applications, layered architectures are routinely employed (e.g., safety or laminated glass) to enhance their mechanical performance. The ability of these materials to bear load, absorb energy, and remain transparent upon impact is critical especially when human lives and critical instruments are involved [1, 2]. Hence, it is essential that the mechanical fracture and failure characteristics of such transparent materials and structures under impact loading conditions are well understood. In this context, a few select layered polymethylmethacrylate (PMMA) architectures are studied in this work since PMMA is an optically transparent structural polymer used as a lightweight alternative in many engineering applications including aerospace applications [3, 4].

In homogenous brittle solids it has been observed that a crack usually propagates under locally mode-I conditions at sub-Rayleigh wave speeds below the crack branching velocity [5, 6]. It is also observed that even when an asymmetric far-field load is imposed, a dynamically growing crack tends to readjust itself to follow a locally mode-I path which makes it physically difficult for it to propagate in mixed-mode or pure mode-II conditions in homogeneous materials [7]. However when a crack grows *along* a weak path in an otherwise homogenous solid, the tendency of the crack to branch or kink out of the weak path is suppressed. This permits the crack to propagate faster than in a monolithic solid at speeds as high as the Rayleigh wave speed [8, 9]. When the crack reaches a

✉ H.V. Tippur
htippur@eng.auburn.edu

¹ Department of Mechanical Engineering, Auburn University, Auburn, AL 36849, USA

critical speed, it is energetically favorable for it to branch and produce multiple crack-tips. An interface if introduced in such a homogeneous material can in principle interfere with the crack propagation [10]. Depending on its properties relative to the parent material, the interface could alter the mechanics of fracture. A crack may arrest at or get trapped in the interface depending on the direction of growth relative to the interface [11]. Further, a crack trapped in an interface with its fracture toughness distinctly different from the adjoining materials has a tendency to branch, kink, or propagate straight ahead depending on factors including the toughness of the interface relative to that of the joined materials. If the interface has a lower fracture toughness relative to the adjoining materials, the crack tends to propagate as a trapped mixed-mode crack. The dissimilarity in the moduli of the joined materials, loading asymmetry, and geometry also contribute to the mode-II component in such scenarios [11–13]. Whether the crack advances along the interface or kinks out of the interface depends on the fracture toughness of the interface relative to that of the joined solids.

From the above review it is evident that an interface greatly affects the crack growth behavior. Previous studies have reported mixed-mode dynamic crack growth involving interfaces using photoelasticity [7, 12, 14, 15] and/or high-speed photography [13]. Coherent Gradient Sensing (CGS) has also been used to study dynamically loaded stationary crack-tips [16] as well as propagating crack problems [17–19]. One of the earliest studies on dynamic interface crack growth was carried out by Tippur and Rosakis [17] using CGS wherein they reported unusually high crack velocities approaching the Rayleigh wave speed of the more compliant constituent of a bi-layered dissimilar material as the crack propagated along an interface. Subsequent investigations showed that the interfacial crack speeds could become intersonic [7, 9, 20] and supersonic [21, 22] in such bimetals. Xu and Rosakis [14] have visualized different modes of failure in homogeneous but layered configurations subjected to impact loading and reported various failure mechanisms involving inter-layer and intra-layer cracking. Further, Xu et al. [7] have examined the effect of interface angle and its strength in a homogeneous bi-layered system with an inclined interface on crack penetration/deflection mechanisms. They have reported that the angle of incidence of the crack relative to the interface plays a significant role in its penetration vs. deflection mechanisms. In a similar study by Chalivendra and Rosakis [12], the effect of crack velocity as it approaches the interface at an inclination has been examined. Another recent study by Park and Chen [13] reports crack growth visualization in glass using high-speed photography. Specifically, they have

observed several interesting effects when a crack impinges normally on an interface and its subsequent growth behavior.

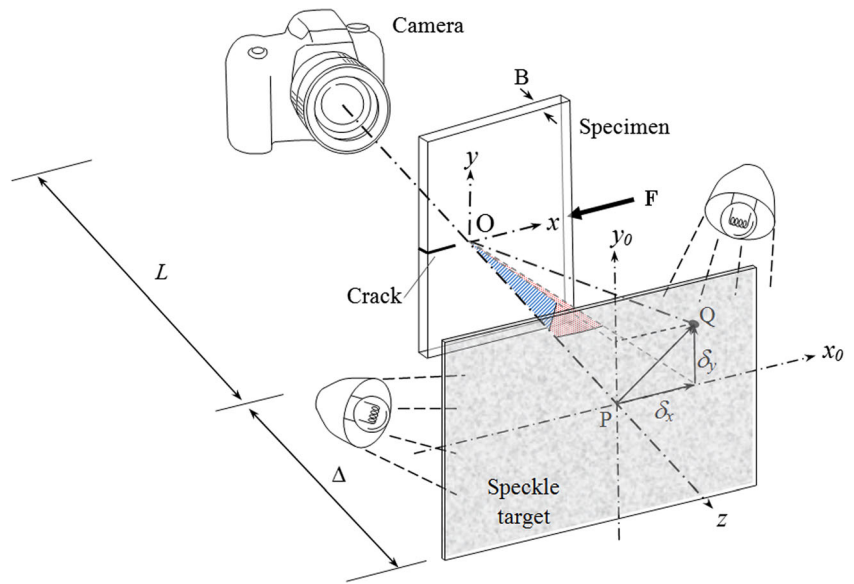
Though many of the above mentioned studies have dealt with the visualization of crack initiation and growth along interfaces, quantitative examination of a dynamically growing crack approaching a normal interface, subsequent growth along the interface, and branching into the next layer is sparse. Hence, the mechanics of a dynamically growing crack entering and exiting an interface besides growing within an interface in terms of crack velocities and fracture parameter histories needs further insight. This paper attempts to shed some light on these aspects by examining the dynamic fracture of bi-layered PMMA sheets. A relatively new full-field optical technique—Digital Gradient Sensing (DGS) [23, 24]—is implemented to visualize dynamic crack propagation and quantify crack-tip parameters under mode-I as well as mixed-mode conditions. Further, dynamic fracture behavior of layered PMMA is comparatively studied relative to monolithic counterparts to bring out the effects of an interface.

In the ensuing sections, the principle behind DGS and the associated methodology employed in this work is briefly described. First, the DGS technique is demonstrated for studying mixed-mode crack problems using an edge cracked strip subjected to far-field uniform tension. Next, the bi-layered specimen preparation, interface characterization, DGS experimental setup and the dynamic testing procedures are explained. This is followed by experimental observations and results including fractured samples, stress gradient contours and fracture parameters such as crack length, crack velocity, mixed-mode stress intensity factor and energy release rate histories. Finally, the major findings of the current study are discussed and summarized.

Digital Gradient Sensing

A schematic for the experimental setup for transmission-mode DGS is shown in Fig. 1. In transmission mode DGS [23, 24] a random speckle pattern on a planar surface, referred to as the ‘target’, is photographed through a planar, optically transparent sheet being studied. White light illumination is used for recording random gray scales on the target. The speckle pattern is first photographed through the specimen in its undeformed state to obtain a reference image. That is, a point P on the target plane ($x_0 - y_0$ plane) is recorded by the camera through point O on the specimen plane ($x - y$ plane). Upon loading, the non-uniform stresses due to the imposed loads change the refractive index of the specimen in the crack-tip vicinity. Additionally, the Poisson effect produces non-uniform thickness changes. A combination of these, commonly known as the *elasto-optic effect*, causes the light rays to deviate from their original path as they propagate in the crack-tip vicinity. The speckle pattern is once again

Fig. 1 The schematic of the experimental setup for Digital Gradient Sensing (DGS) technique to determine planar stress gradients in phase objects [24]



photographed through the specimen in the deformed state. Then a neighboring point Q on the target plane is recorded by the camera through point O on the specimen plane after deformation. The local deviations of light rays can be quantified by correlating speckle images in the deformed and

reference states to find displacement components δ_x and δ_y . The angular deflections of light rays ϕ_x and ϕ_y in two orthogonal planes (x - z and y - z planes with the z -axis coinciding with the optical axis of the setup and x - y being the specimen plane coordinates) can be computed if the distance between the

Fig. 2 Analytical contour plots of ϕ_x and ϕ_y for (a) $K_{II}=0$ and (b) $K_I/K_{II}=4$. The numerical values on the contours represent relative magnitudes and sign of DGS contours

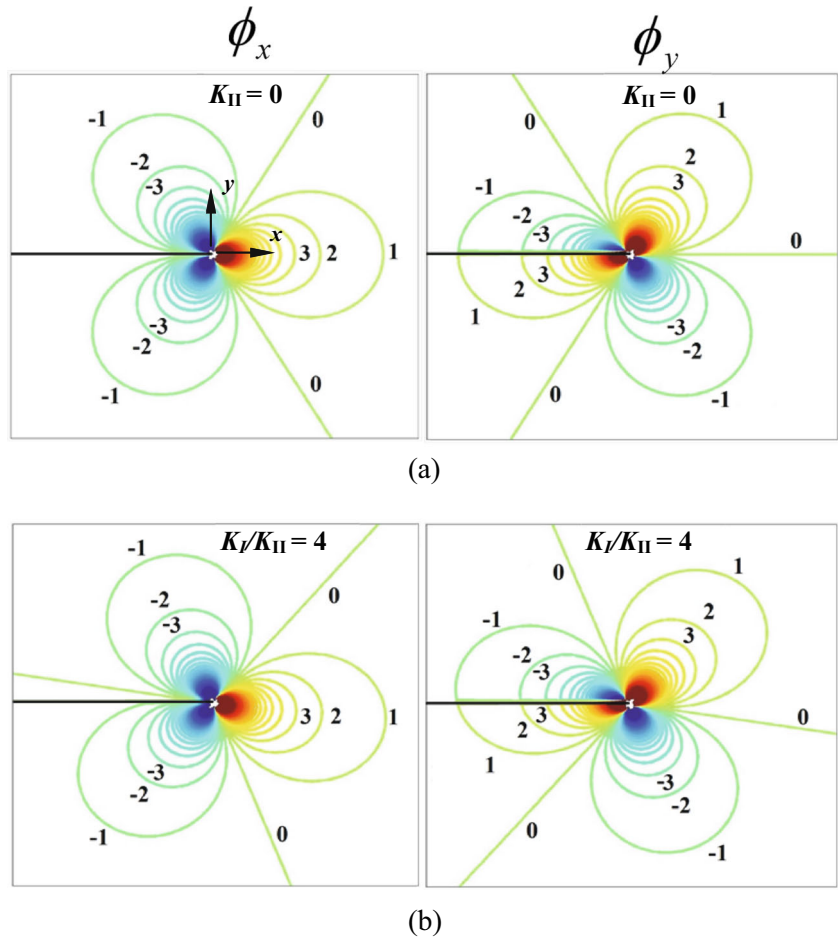


Table 1 Some properties and dimensions of cast PMMA used [23, 24]

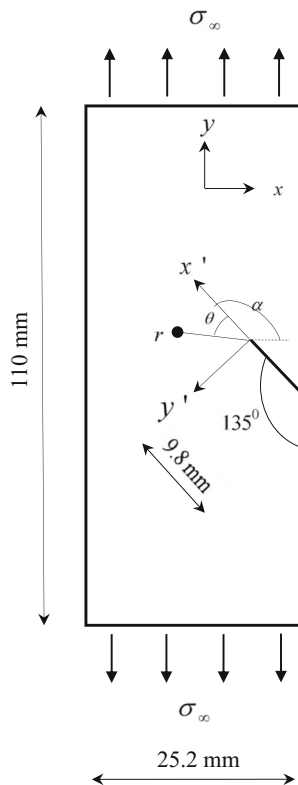
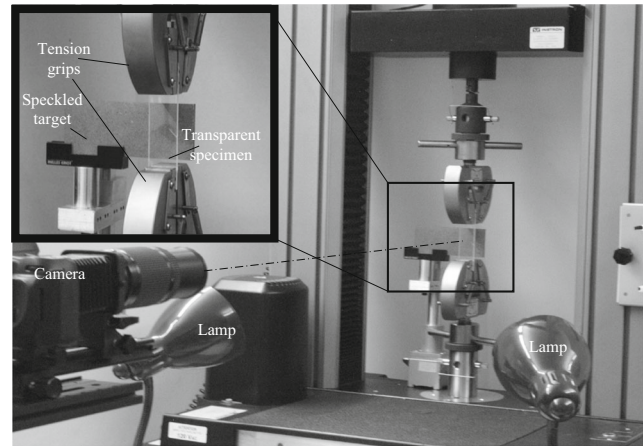
Parameter	Static value	Dynamic value
Density	1010 kg/m ³	1010 kg/m ³
Elastic modulus	3.3 GPa	5.0 GPa
Poisson's ratio	0.34	0.34
Elasto-optic constant	-0.9×10^{-10} m ² /N	-1.08×10^{-10} m ² /N
Thickness	4.5 mm	8.6 mm

specimen plane and the target plane is known. A detailed analysis under paraxial conditions by Periasamy and Tippur [24] shows that the local angular deflections are related to the gradients of in-plane normal stresses as,

$$\phi_x = C_\sigma B \frac{\partial(\sigma_x + \sigma_y)}{\partial x} = C_\sigma B \frac{\partial I_1}{\partial x} \quad (1)$$

$$\phi_y = -C_\sigma B \frac{\partial(\sigma_x + \sigma_y)}{\partial y} = -C_\sigma B \frac{\partial I_1}{\partial y} \quad (2)$$

where C_σ is the elasto-optic constant of the material, B is its initial thickness and $I_1 = (\sigma_x + \sigma_y)$ is the first invariant of stress for plane stress condition and σ_x and σ_y denote thickness wise averages.

**Fig. 3** Specimen geometry used for quasi-static mixed-mode tension experiment**Fig. 4** Experimental setup used for measuring mixed-mode crack tip fields in a tensile strip using DGS. Inset shows close-up view of the edge cracked specimen and the target

Using asymptotic expansion for I_1 in Equation (1), expressions for angular deflections in case of a mode-I static crack-tip become [25, 26],

$$\phi_x = C_\sigma B \frac{\partial I_1}{\partial x} = C_\sigma B \sum_{N=1}^{\infty} A_N \left(\frac{N}{2}-1\right) r^{\left(\frac{N}{2}-2\right)} \cos\left(\left(\frac{N}{2}-2\right)\theta\right) \quad (3)$$

$$\phi_y = -C_\sigma B \frac{\partial I_1}{\partial y} = -C_\sigma B \sum_{N=1}^{\infty} A_N \left(\frac{N}{2}-1\right) r^{\left(\frac{N}{2}-2\right)} \sin\left(\left(\frac{N}{2}-2\right)\theta\right) \quad (4)$$

Similarly, expressions for angular deflections in case of a mixed-mode (mode-I + -II) static crack-tip are [20],

$$\begin{aligned} \phi_x &= C_\sigma B \frac{\partial I_1}{\partial x} \\ &= C_\sigma B \sum_{N=1}^{\infty} \left\{ A_N \left(\frac{N}{2}-1\right) r^{\left(\frac{N}{2}-2\right)} \cos\left(\left(\frac{N}{2}-2\right)\theta\right) \right. \\ &\quad \left. + D_N \left(\frac{N}{2}-1\right) r^{\left(\frac{N}{2}-2\right)} \sin\left(\left(\frac{N}{2}-2\right)\theta\right) \right\} \quad (5) \end{aligned}$$

$$\begin{aligned} \phi_y &= -C_\sigma B \frac{\partial I_1}{\partial y} \\ &= -C_\sigma B \sum_{N=1}^{\infty} \left\{ A_N \left(\frac{N}{2}-1\right) r^{\left(\frac{N}{2}-2\right)} \sin\left(\left(\frac{N}{2}-2\right)\theta\right) \right. \\ &\quad \left. - D_N \left(\frac{N}{2}-1\right) r^{\left(\frac{N}{2}-2\right)} \cos\left(\left(\frac{N}{2}-2\right)\theta\right) \right\} \quad (6) \end{aligned}$$

where (r, θ) denote the crack-tip polar coordinates, $A_1 = K_I \sqrt{\frac{2}{\pi}}$ with K_I being mode-I stress intensity factor (SIF) and $D_1 = K_{II} \sqrt{\frac{2}{\pi}}$ with K_{II} being mode-II stress intensity factor. Using the above analytical expressions (3)–(6) with $N=1$, the angular deflection contours are plotted as shown in Fig. 2 for a mode-I and a mixed-mode case. The tri-lobed contours with 120° symmetry

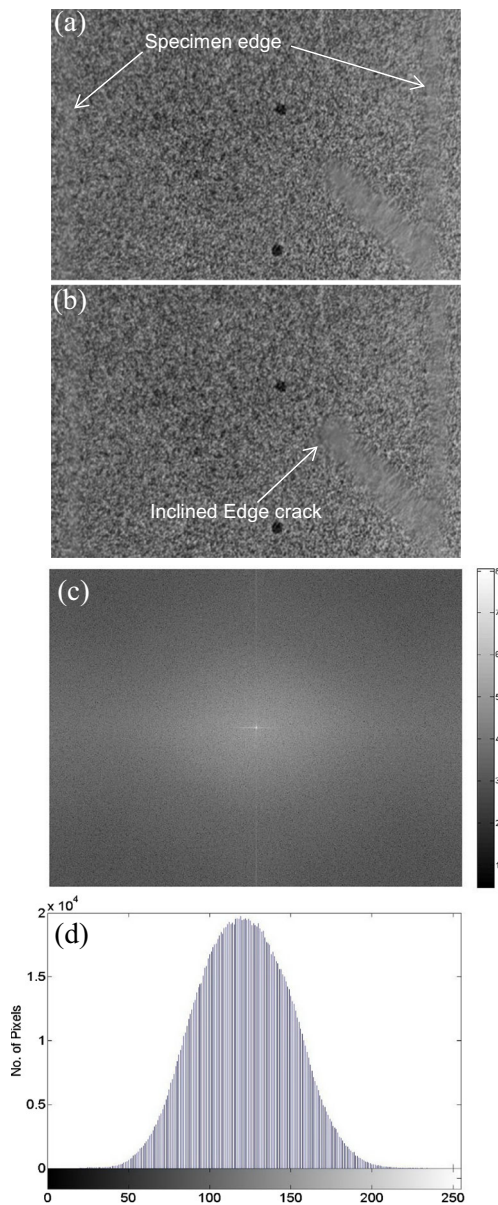


Fig. 5 Speckle image of the target plate through the transparent edge cracked specimen at (a) no-load and (b) far-field stress $\sigma_\infty \approx 6$ MPa. The two black dots are 10 mm apart. (c) Logarithm of the absolute of the magnitude of FFT of the speckle pattern. (d) The histogram of the speckle pattern

relative to the crack axis for ϕ_x and asymmetry for ϕ_y in case of mode-I is evident in Fig. 2(a). For the mixed-mode case on the other hand, the contours rotate relative to the crack axis as shown in Fig. 2(b). These contours were generated using only the K -dominant terms in the asymptotic expressions and hence the size of each set of lobes are identical. However, in finite geometries and/or transiently varying states of stress, the size of each set of lobes could be different due to the presence of higher order terms ($N > 1$).

Overall Experimental Approach

In this study, the proposed approach was first calibrated using a quasi-static mixed-mode tension experiment using transmission-mode DGS. A series of photographs of random speckle pattern on a target plate was recorded through a rectangular tension specimen with an inclined edge crack. Initial image was recorded in the undeformed state and subsequent images were recorded as the specimen was loaded. Using 2D-DIC (Digital Image Correlation) these images were correlated with the reference image (in the undeformed state) to obtain data representing ϕ_x and ϕ_y . From these orthogonal angular deflections, mode-I and mode-II SIF values for each image were evaluated using an over-deterministic full-field data analysis. A finite element (FE) analysis of this experiment was also carried out. Using regression analysis on crack opening and crack sliding displacements, the mode-I and mode-II SIFs were evaluated during FE simulations.

Subsequently, this approach was extended to study dynamic mixed-mode crack propagation across interfaces in bilayered specimens. The geometry and loading configurations were inspired from similar studies reported in the past [12–15, 27]. Yet, the sample size was relatively smaller due to the need to control interface thickness (to be discussed later on). Again, the random speckle pattern was recorded through the transparent specimen during the transient event using an ultrahigh-speed digital camera. Thirty-two pairs of images, each pair containing one image each from the undeformed and deformed states, were recorded. Each image pair was analyzed separately to obtain full-field DGS data as a rectangular array in the region of interest. This was repeated for all 32 sets of images. From this, angular deflections in two orthogonal directions and subsequently SIF histories were evaluated. The details regarding these are reported in the following sections.

Quasi-Static Mixed-Mode Crack

Specimen Preparation and Geometry

A 110 mm \times 25.2 mm rectangular specimen of 4.5 mm thickness was machined from a cast PMMA sheet. Some of the relevant properties of PMMA used in this study are listed in Table 1. A 45° inclined edge notch of length 9.8 mm was introduced into the specimen as shown in Fig. 3 using a diamond impregnated circular saw of approximately 300 μ m thickness. The crack-tip was sharpened by scoring the notch tip with a fresh razor blade. The target plate used for DGS measurements was prepared by spraying a fine mist of black and white paints successively on a flat surface to create random speckles. Two heavy black dots were marked 10 mm apart on the target plate to relate the spatial dimensions on the image to those on the target plate and the specimen.

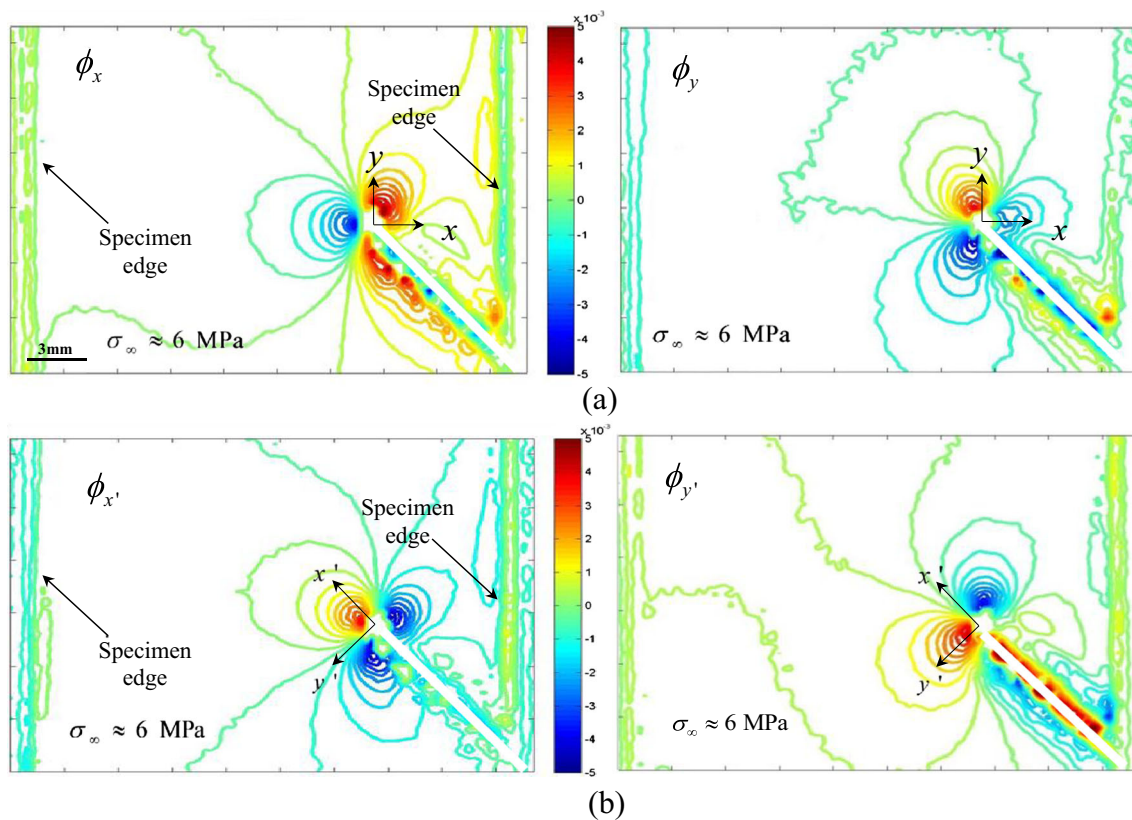


Fig. 6 (a) The Angular deflection contours (contour interval= 4×10^{-4} rad) around the mixed-mode crack tip in (a) global coordinates (x - y coordinate system) for a representative load level obtained from DGS. The contours on the left represent ϕ_x (in the x - z plane) and the contours on

the right represent ϕ_y (in the y - z plane) (b) local coordinate system (x' - y' coordinate system) for a representative load level obtained from DGS. The contours on the left represent $\phi_{x'}$ (in the x - z plane) and the contours on the right represent $\phi_{y'}$ (in the y - z plane)

Experimental Setup and Procedure

A photograph of the experimental setup used to demonstrate DGS to study mixed-mode crack problems is shown in Fig. 4. An Instron 4465 universal testing machine was used for loading the specimen in tension and in displacement control mode (crosshead speed=0.005 mm/sec). The speckled target plate was located at a distance of $\Delta=27.3$ mm from the specimen mid-plane behind the specimen. A Nikon D100 digital SLR camera fitted with a 70–300 mm focal length lens (with an aperture setting of F22) and an extension tube was used to record the speckles. The camera was placed in front of the specimen at a distance (L) of approximately 1400 mm with the camera focused on the target through the specimen. Both the camera and the testing machine were controlled using a computer. Two regular incandescent lamps were used to illuminate the target plate uniformly. Incandescent light source compensation setting was used to account for the yellowness of the light source. During recording, a camera resolution of 1504×1000 pixels was used to acquire 8 bit images.

A reference/undeformed image of the target plate speckles through the crack-tip vicinity was recorded in no-load (load < 1 N) condition. As the sample was loaded gradually, the

perturbed images of the target plate were recorded using time-lapse photography at 20 frames per minute. Two representative speckle patterns, one in the reference state and the other in the deformed state, are shown in Fig. 5. The recorded images correspond to $30 \text{ mm} \times 20 \text{ mm}$ region on the specimen. Using a pair of heavy black dots (see, Fig. 5(a) and (b)) marked on the target plate, the dimensions on image in terms of pixels were related back to specimen/target plate dimensions (1 pixel=approx. $20 \mu\text{m}$ on the target plane). Sufficient care was also exercised to obtain a near Gaussian distribution of gray scales for each image in the mid-range of 0–255 (8 bit) scale by positioning the lamps appropriately. When examined carefully, it can be seen that the speckles are noticeably smeared in Fig. 5(b) in the vicinity of the stress concentration (particularly ahead of the crack-tip) whereas the speckles are largely unaffected in the far-field.

Image Analysis

The 2D-DIC was carried out using ARAMIS® software. A facet/sub-image size of 25×25 pixels with an overlap of 10 pixels (i.e., step size of 15 pixels) was used during speckle correlation. Each speckle covered approximately 9–10 pixels. The resulting data matrix of size

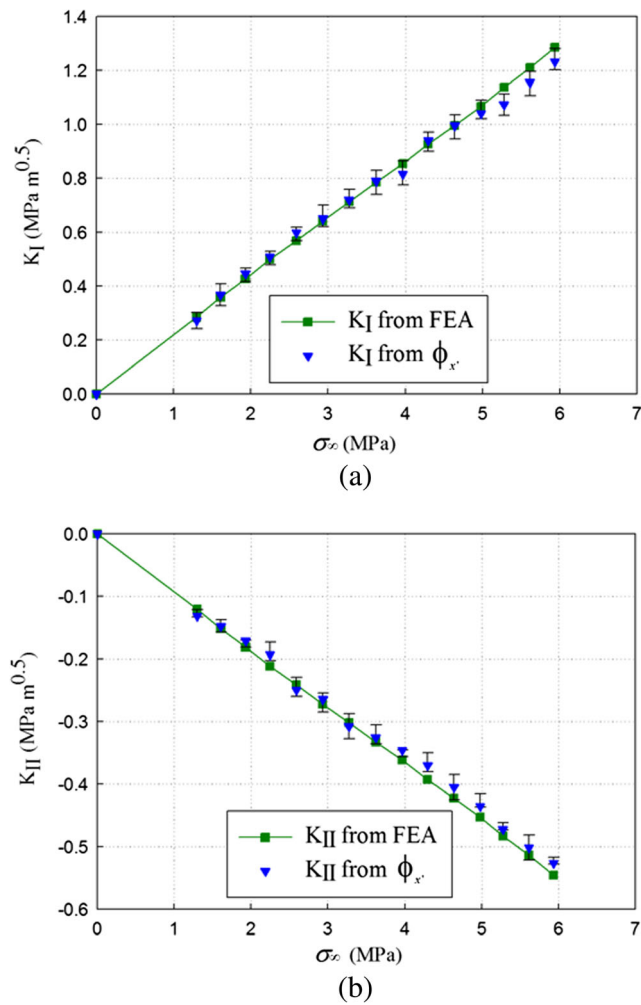


Fig. 7 Variation of measured mixed-mode SIFs with far-field stress and comparison with FE counterparts. (a) K_I (b) K_{II}

64×98 was exported to MATLAB for post-processing including the evaluation of orthogonal angular deflections in the region of interest. The angular deflection contours in the horizontal (x - z) and vertical (y - z) planes (global coordinate system) for a select far-field uniform

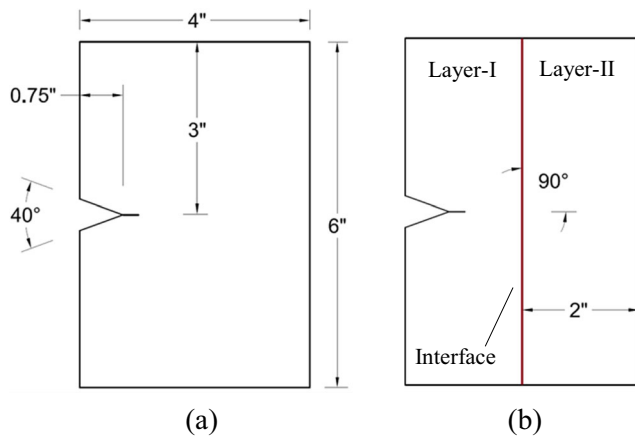


Fig. 8 Specimen configurations studied. (a) Monolithic (b) Bi-layered

Table 2 Characteristics of Weldon 16 acrylic adhesive

Adhesive properties and characteristics	
Parameter	Value
Color	Clear
Viscosity	800 cps
Working time	2–3 min
Fixure time	5–6 min
80 % strength	16 h
Specific gravity	1.02±0.04

tension of 6 MPa is shown in Fig. 6(a). A heavy white line is overlaid on the resulting contours to represent the edge crack.

Evaluation of SIFs

To facilitate analyzing DGS data in the local crack-tip coordinates (x' and y'), the corresponding angular deflections $\phi_{x'}$ and $\phi_{y'}$ were expressed in terms of ϕ_x and ϕ_y in the global coordinates (x, y) using the transformation angle α as,

$$\phi_{x'} = \phi_x \cos \alpha + \phi_y \sin \alpha \tag{7}$$

$$\phi_{y'} = -\phi_x \sin \alpha + \phi_y \cos \alpha \tag{8}$$

Now, the angular deflections for a mixed-mode static crack-tip can be expressed in the local coordinates as,

$$\phi_{x'} = C_\sigma B \frac{\partial I_1}{\partial x'} = C_\sigma B \sum_{N=1}^{\infty} \left\{ \begin{aligned} &A_N \left(\frac{N}{2}-1\right) r^{\left(\frac{N}{2}-2\right)} \cos\left(\left(\frac{N}{2}-2\right)\theta\right) \\ &+ D_N \left(\frac{N}{2}-1\right) r^{\left(\frac{N}{2}-2\right)} \sin\left(\left(\frac{N}{2}-2\right)\theta\right) \end{aligned} \right\} \tag{9}$$

$$\phi_{y'} = -C_\sigma B \frac{\partial I_1}{\partial y'} = -C_\sigma B \sum_{N=1}^{\infty} \left\{ \begin{aligned} &A_N \left(\frac{N}{2}-1\right) r^{\left(\frac{N}{2}-2\right)} \sin\left(\left(\frac{N}{2}-2\right)\theta\right) \\ &- D_N \left(\frac{N}{2}-1\right) r^{\left(\frac{N}{2}-2\right)} \cos\left(\left(\frac{N}{2}-2\right)\theta\right) \end{aligned} \right\} \tag{10}$$

where $I_1 = (\sigma_x + \sigma_y) = (\sigma_{x'} + \sigma_{y'})$ is used and (r, θ) denote polar coordinates defined as shown in Fig. 3, C_σ is the elastooptic constant of PMMA, $B=4.5$ mm is the initial thickness of the specimen, $A_1 = K_I \sqrt{\frac{2}{\pi}}$ with K_I being the mode-I stress intensity factor and $D_1 = K_{II} \sqrt{\frac{2}{\pi}}$ with K_{II} the mode-II stress intensity factor. In this experiment, the SIFs were evaluated using Equation (9) by employing an overdeterministic regression analysis of the measured data and

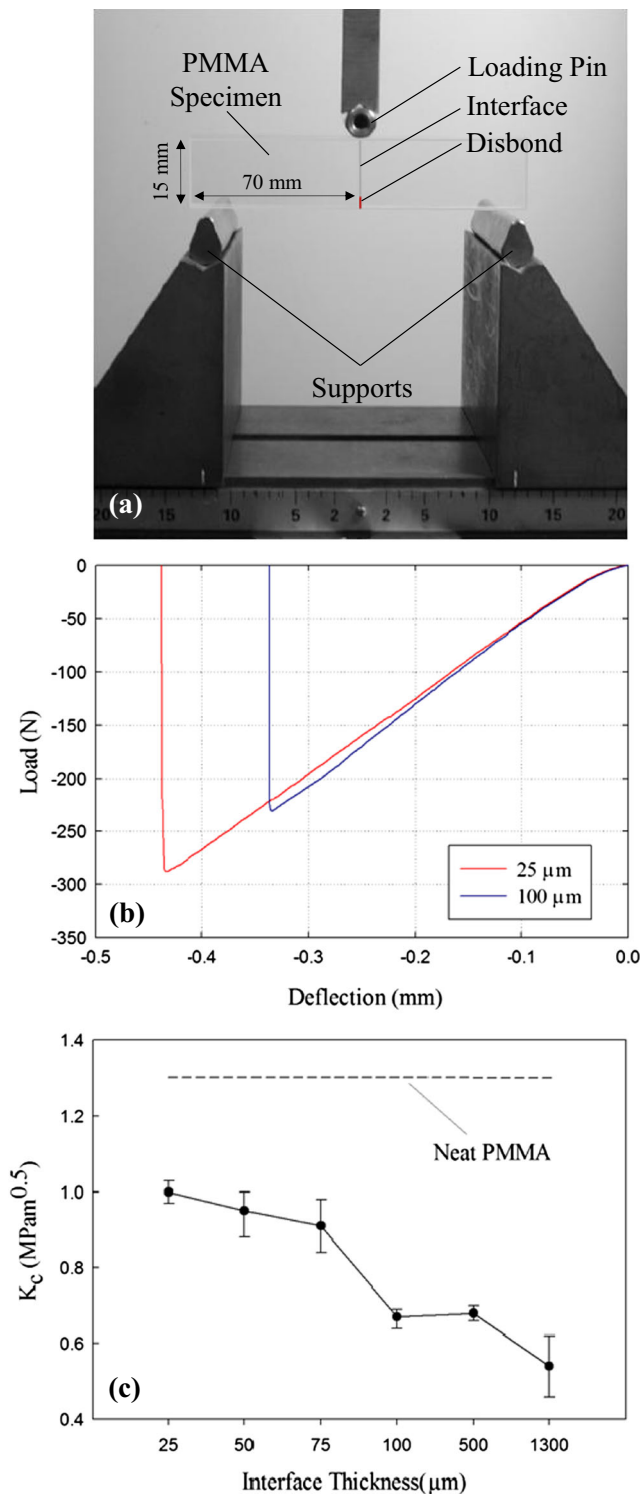


Fig. 9 (a) Photograph of the experimental setup for the interface characterization. (b) Measured load-deflection response for fracture specimens with 25 μm and 100 μm interface thicknesses. (c) Variation of crack initiation toughness with interface thickness. (Note that all interfaces have lower crack initiation toughness than the virgin material.)

$N=4$. (Alternatively, Equation (10) can also be used to evaluate the SIFs; results presented here are based on Equation (9)). Discrete angular deflection values around

the crack-tip in the region $0.4 \leq r/B \leq 1.5$ and $-135^\circ \leq \theta \leq 135^\circ$ were used in the regression analysis. This ensured that the data used was sufficiently close to the crack-tip yet outside the region of dominant triaxial effects near the crack-tip [18]. This also indirectly helped in minimizing the error in locating the crack-tip due to the edge effects introduced by the image correlation operation.

Experimental Results

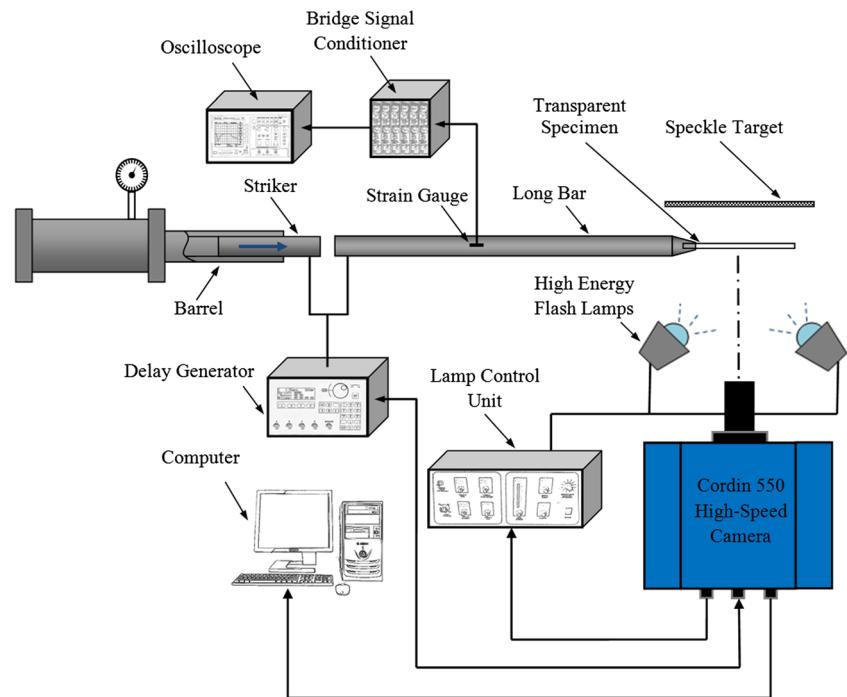
Figure 6(b) shows the orthogonal angular deflection plots for a select far-field stress ($\sigma_\infty \sim 6$ MPa) in the local coordinate system (x' and y'). A heavy white line is overlaid on the resulting contours to represent the edge crack. It should be noted that the contour lines adjacent to the crack faces and specimen edges show unavoidable edge effects. It can be seen that the angular deflection contours in the local coordinate system $\phi_{x'}$ and $\phi_{y'}$ have similarities with the analytical angular deflection contours for mixed-mode crack shown in Fig. 2(b). The variation of SIFs obtained from the regression analysis of measured data with the far-field stress (σ_∞) levels are plotted in Fig. 7. The error bars correspond to the SIFs obtained by using different subsets in $0.4 \leq r/B \leq 1.5$ and $-135^\circ \leq \theta \leq 135^\circ$ range. A complimentary FE analysis was also carried out for this experiment and SIFs were evaluated as described in Appendix 1. The SIFs evaluated from the numerical simulation is superimposed on the measured SIFs in Fig. 7. A good agreement between the two is clearly evident.

Dynamic Crack Propagation in Bi-Layered Specimens

Specimen Geometry and Preparation

Two different specimen geometries were used in this study and are shown in Fig. 8. One of the geometries is for a monolithic specimen whereas the other is a bi-layered geometry. The layered specimen was prepared by bonding two PMMA sheets (152 mm \times 50.8 mm of thickness 8.6 mm) using a commercially available acrylic adhesive, Weldon 16, whereas the monolithic specimen was a single PMMA sheet (152.4 mm \times 101.6 mm of thickness 8.6 mm). In case of layered configurations, bonding surfaces of the constituent layers underwent additional surface preparation prior to bonding. They were first sanded using 400-grit sandpaper in the direction perpendicular to the thickness of the specimen and then cleaned using lint free cloth soaked in isopropyl alcohol to remove any residue. The two layers to be bonded were placed on the bed of a drill press vise. The adhesive was applied to one of the two bonding surfaces and both the surfaces were squeezed against each other using the jaws

Fig. 10 Schematic of the experimental setup used for dynamic fracture study (*top view*)



of the vise. Steel spacers of required thickness were placed between the two layers to control the resulting interface thickness. The joint was cured for 24 h before experimentation. The adhesive characteristics and properties are shown in Table 2. The properties of PMMA sheet are shown in Table 1. A 40° V-notch was machined on one edge of both monolithic and bi-layered specimens and was subsequently extended into the specimen for 2 mm. The extended notch was sharpened by scoring with a sharp razor blade. The wedge shaped end of the long impactor bar (see Fig. 11) matched the V-notch of each of these specimens. The overall dimensions of both monolithic and layered specimens were the same.

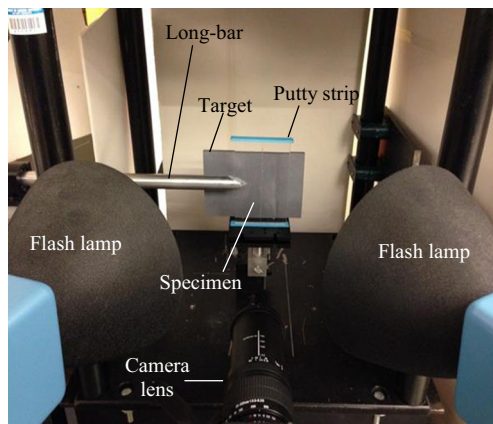


Fig. 11 Photograph of the close-up view of the experimental setup used in dynamic fracture experiments

Interface Characterization

The interface was characterized by its quasi-static crack initiation toughness. Three-point bend tests on edge cracked geometry were used for this purpose. Two rectangular PMMA pieces of $70 \text{ mm} \times 15 \text{ mm}$ and thickness of 8.6 mm (see Fig. 9(a)) were bonded together to form the test specimen. The bonding surfaces ($8.6 \text{ mm} \times 15 \text{ mm}$) were prepared similar to the one used for preparing dynamic fracture specimens. The adhesive (Weldon 16) was applied to one of the surfaces, and the two pieces were held in the drill press vise to bond the surfaces. A pair of steel spacers of known thickness was placed between the bonding surfaces to obtain required bond thickness. Specimens with various bond layer thicknesses from $25 \mu\text{m}$ to 1.3 mm were prepared and were used to make multiple $70 \text{ mm} \times 15 \text{ mm}$ fracture specimens from each plate to measure interfacial crack initiation toughness. A 3 mm long disbond was introduced along the interface of each sample during preparation. The specimen was left in the vise for 24 h before performing the fracture tests.

An Instron 4465 loading machine was used to perform symmetric 3-point bend tests. The specimen was loaded in displacement control mode with a cross-head speed of 0.005 mm/sec. The load was applied on the interface of the edge cracked beam samples (span=120 mm) as shown in Fig. 9(a). The applied load history was recorded up to fracture. Representative load deflection plots for two select interface thicknesses are shown in Fig. 9(b). The samples fractured in a brittle fashion and from the measured peak load and the

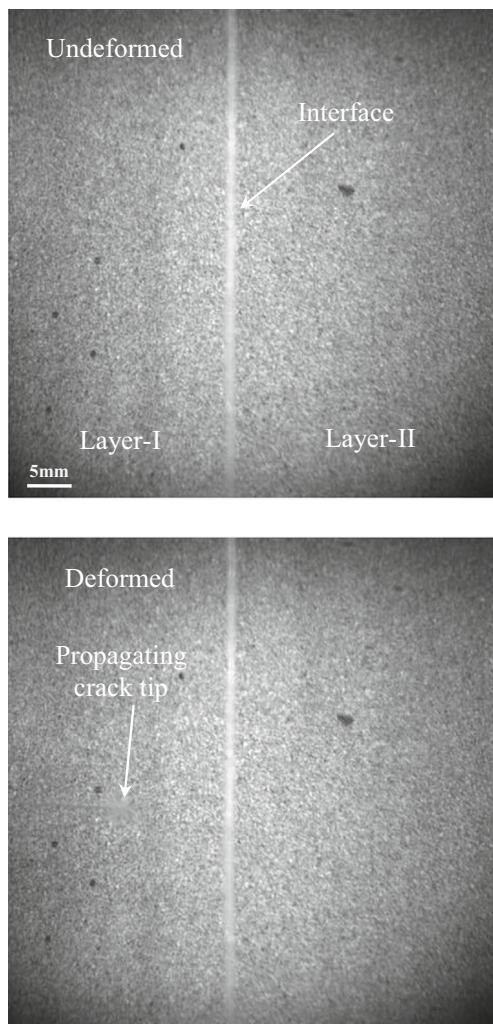


Fig. 12 Speckle images in the undeformed (*top*) and deformed (*bottom*) states recorded by the high-speed camera through the bi-layered PMMA specimen

specimen geometry the crack initiation toughness was evaluated using Equation (11) [26]:

$$K_I = \frac{FS}{Bw^{3/2}} \frac{3(\xi)^{1/2} [1.99 - \xi(1-\xi) \{2.15 - 3.93(\xi) + 2.7(\xi)^2\}]}{2(1+2\xi)(1-\xi)^{3/2}}, \quad \xi = \frac{a}{w} \quad (11)$$

where, F is the peak load applied, S is the span, B is the thickness of the specimen, w is the width of the specimen and a is the initial crack length.

This was repeated for various interface thicknesses to estimate the dependence of crack initiation toughness on interface thickness. The results thus obtained are plotted in Fig. 9(c) for different interface thicknesses. From the plot, it can be seen that the crack initiation toughness decreases with the interface thickness, especially after 75 μm . Two cases, one with an interface thickness of 25 μm and another with 100 μm were chosen as the ‘strong’ and ‘weak’ interfaces, respectively. The critical static mode-I SIF for neat PMMA was also measured

using symmetric 3-point bend tests and was recorded as $1.31 \pm 0.07 \text{ MPa}\sqrt{\text{m}}$ (dotted line in Fig. 9(c)) which is *higher than the crack initiation toughness of both the interface thicknesses studied*. The weak and strong interface toughness were $\sim 52\%$ and $\sim 77\%$, respectively, of virgin PMMA.

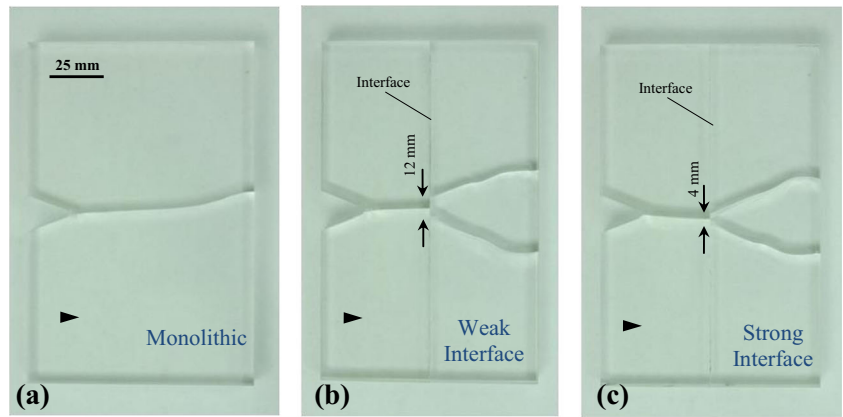
Experimental Setup and Procedure

Dynamic fracture study of monolithic and layered PMMA specimens was carried out in conjunction with DGS technique and ultrahigh-speed digital photography. The schematic of the experimental setup used is shown in Fig. 10. A Hopkinson pressure bar was used for loading the specimen. It included a 6 ft long cylindrical bar of 1 in. diameter with a polished wedge shaped tip held against the unconstrained specimen with an identical wedge shaped V-notch (see, Fig. 8). A 12 in. long, 1 in. diameter rod held inside the barrel of a gas-gun was co-axially aligned with the long-bar and was used as the striker. Both the long-bar and the striker-bar were made of AL 7075-T6 eliminating any impedance mismatch between them.

The image acquisition system included a Cordin-550 ultra-high-speed digital camera capable of recording images at a maximum rate of up to 2 million frames per second at a resolution of 1000×1000 pixels on 32 independent CCD sensors positioned radially around a five-facet rotating mirror. The imaging system also included two high-energy flash lamps producing broad-band white light illumination. Experimental parameters such as trigger delay, flash duration, framing rate, the CCD gain and image storage were controlled using a computer connected to the camera. A 28–300 mm focal length macro zoom lens along with an adjustable bellows were used for imaging. Further, an aperture setting of F5.6 was selected to achieve a good exposure and focus with minimum gain setting for signal amplification during high-speed imaging. The specimen was at a distance of approximately 900 mm in front of the camera. The specimen was placed on a flat adjustable platform with a layer of putty on the top and bottom edges of the specimen, as shown in Fig. 11. The putty was placed to achieve similar and ‘free’ boundary conditions at the top and bottom surfaces of the specimen. A target plate with random black and white speckles was placed behind the specimen at a fixed distance $\Delta = 29.3$ mm away from the mid-plane of the specimen to perform DGS measurements. A pair of heavy black dots (see Fig. 12) were marked on the target plate to relate the dimension on the image to the actual specimen/target dimensions. The vertical long edge of the specimen containing the V-notch was held against the wedge shaped tip of the long-bar.

The region of interest in this study was around the interface; hence the camera was focused on a square region of 52 mm \times 52 mm in the vicinity of the vertical interface and on both of its sides. Prior to loading, a set of 32 images

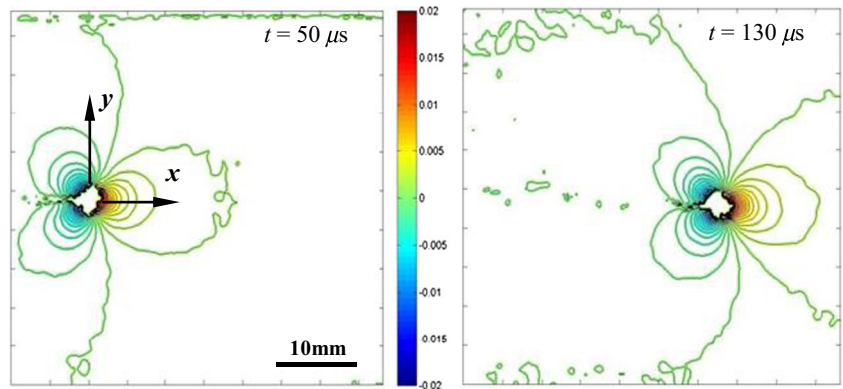
Fig. 13 Photographs of fractured specimens showing crack path selection in (a) Monolithic (b) ‘Weak’ layered configuration (c) ‘Strong’ layered configuration. Arrowhead indicates crack growth direction



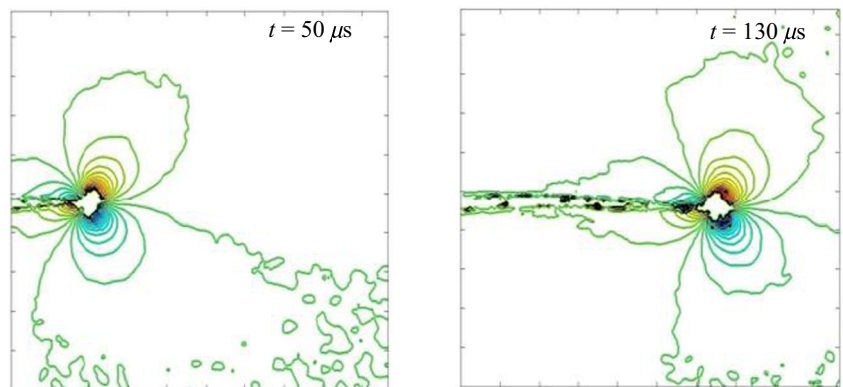
of the target plate through the specimen in the undeformed state were recorded at 200,000 frames per second and stored. Sufficient care was also taken to obtain an approximately Gaussian distribution of gray scales for each image, typically in the mid-range of 0–255 (8 bit) scale by positioning the lamps appropriately. Without changing any camera settings, the striker was launched towards the long-bar using the gas-gun at a velocity of ~15 m/s. When the striker contacted the long-bar, a compressive stress wave

was generated in the long-bar, which propagated along its length before loading the specimen along the two inclined faces of the V-notch. The duration of the stress wave pulse generated was ~107 μ s. When the striker contacted the long-bar, a trigger signal was also generated. This initiated recording of a second set of 32 images (deformed state) at the same framing rate at a preset trigger delay of 445 μ s. Thus, a total of 32 pairs of images in the deformed and undeformed states were recorded at 5 μ s intervals between

Fig. 14 Angular deflection contour plots (contour interval = 8×10^{-4} rad) proportional to stress-gradients in the x - and y -directions for a monolithic specimen. (Crack growth from left to right)



(a) ϕ_x Contours



(b) ϕ_y Contours

successive images. Two representative speckle images recorded through the specimen in the region of interest, one in the undeformed state and the other in deformed state for a layered specimen configuration, is shown in Fig. 12. It can be seen that the speckles are noticeably smeared in the vicinity of the propagating crack-tip (in the deformed image) whereas they are largely unaffected in the far-field. The interface is seen as a translucent vertical line at the centre of each image. The corresponding two images for each sensor were paired from the undeformed and deformed sets and each of these 32 matched pairs were correlated individually.

Image Analysis

The 2D-DIC was again carried out using the image analysis software ARAMIS[®]. The recorded image corresponds to approximately 52×52 mm² region on the specimen. Each image was segmented into facets/sub-images consisting of 25×25 pixels during analysis. An overlap of 20 pixels (i.e. step size of 5 pixels) was used during image correlation. Each speckle covered approximately 4–5 pixels. This resulted in 194×194 matrix of data points in the region of interest for each of the two orthogonal angular deflection fields. Using MATLAB, in-plane orthogonal deflections were evaluated using the known distance Δ between the specimen and the target planes.

Evaluation of Crack Velocities and Stress Intensity Factors

The position of the crack-tip in each digitized image was used to measure the instantaneous crack length. Using the crack length history, crack velocity C was evaluated using backward difference computations. Since two-orthogonal angular deflection fields are available from DGS for a propagating mixed-mode crack, Equations (7)–(8) can be used to rotate the instantaneous angular deflection fields from the global coordinates to the local coordinates (x' and y') along and perpendicular to the current crack-tip orientation as,

$$\phi_{x'}(t) = \phi_x(t) \cos \theta(t) + \phi_y(t) \sin \theta(t) \quad (12)$$

$$\phi_{y'}(t) = -\phi_x(t) \sin \theta(t) + \phi_y(t) \cos \theta(t) \quad (13)$$

Further, Equations (9)–(10) can be modified for a dynamically propagating steady-state¹ crack as [19],

¹ The crack speeds in the interface vicinity show gyrations and hence using transient crack-tip field descriptions [28] involving derivatives of SIF values are more appropriate. However, in view of potential inaccuracies associated with numerical differentiation of SIF values, a steady-state approximation is adopted in this work.

$$\phi_{x'} = C_{\sigma} B \frac{\partial I_1}{\partial x'} = C_{\sigma} B \left[\begin{array}{l} -\frac{1}{2} r_l^{-\frac{3}{2}} \left\{ \begin{array}{l} f(C; C_L; C_S) A_1(t) \cos\left(\frac{3\theta_l}{2}\right) \\ + g(C; C_L; C_S) D_1(t) \sin\left(-\frac{3\theta_l}{2}\right) \end{array} \right\} \\ + \sum_{N=2}^{\infty} \left\{ \begin{array}{l} A_N \left(\frac{N}{2}-1\right) r_l^{\left(\frac{N}{2}-2\right)} \cos\left(\left(\frac{N}{2}-2\right)\theta_l\right) \\ + D_N \left(\frac{N}{2}-1\right) r_l^{\left(\frac{N}{2}-2\right)} \sin\left(\left(\frac{N}{2}-2\right)\theta_l\right) \end{array} \right\} \end{array} \right] \quad (14)$$

$$\phi_{y'} = -C_{\sigma} B \frac{\partial I_1}{\partial y'} = -C_{\sigma} B \left[\begin{array}{l} \frac{1}{2} r_l^{-\frac{3}{2}} \left\{ \begin{array}{l} f(C; C_L; C_S) A_1(t) \sin\left(\frac{3\theta_l}{2}\right) \\ + g(C; C_L; C_S) D_1(t) \cos\left(-\frac{3\theta_l}{2}\right) \end{array} \right\} \\ + \sum_{N=2}^{\infty} \left\{ \begin{array}{l} A_N \left(\frac{N}{2}-1\right) r_l^{\left(\frac{N}{2}-2\right)} \sin\left(\left(\frac{N}{2}-2\right)\theta_l\right) \\ - D_N \left(\frac{N}{2}-1\right) r_l^{\left(\frac{N}{2}-2\right)} \cos\left(\left(\frac{N}{2}-2\right)\theta_l\right) \end{array} \right\} \end{array} \right] \quad (15)$$

where f and g denote functions of instantaneous crack velocity, and (r_l, θ_l) denote the contracted crack-tip polar coordinates for a growing crack. Further, (r_l, θ_l) can be expressed in the local Cartesian coordinates (x', y') as, $r_l = \{(x')^2 + \alpha_L^2 (y')^2\}^{1/2}$ and $\theta_l = \tan^{-1}\left(\frac{\alpha_L y'}{x'}\right)$. The coefficients of $A_1(t)$ and $D_1(t)$ in the asymptotic series are related to mode-I and mode-II stress intensity factors $K_I(t)$ and $K_{II}(t)$, respectively, as

$$A_1(t) = K_I(t) \sqrt{\frac{2}{\pi}} \quad \text{and} \quad D_1(t) = K_{II}(t) \sqrt{\frac{2}{\pi}} \quad (16)$$

For plane stress, the functions f and g are given by [18, 19, 29],

$$f(C; C_L, C_S) = \left(\frac{1+\nu}{1-\nu}\right) \frac{(1+\alpha_S^2)(1-\alpha_L^2)}{4\alpha_L\alpha_S-(1+\alpha_S^2)^2} \quad \text{and} \quad g(C; C_L, C_S) \quad (17)$$

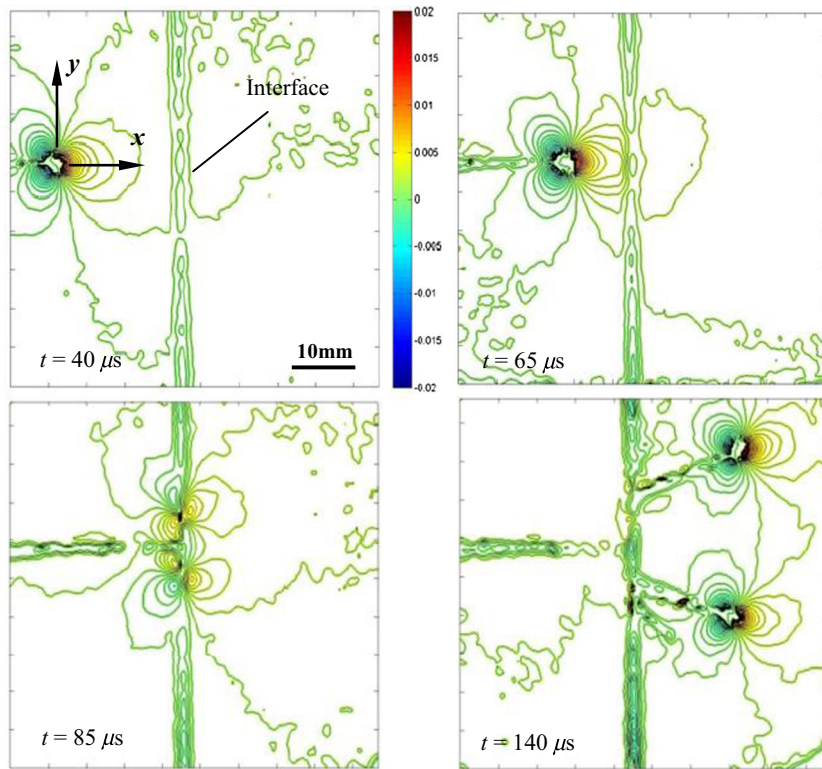
$$= \left(\frac{1+\nu}{1-\nu}\right) \frac{2\alpha_S(1-\alpha_L^2)}{4\alpha_L\alpha_S-(1+\alpha_S^2)^2}$$

where $\alpha_L = \left[1 - \frac{\rho(1-\nu)}{2\mu} C^2\right]^{\frac{1}{2}}$ and $\alpha_S = \left[1 - \frac{\rho}{\mu} C^2\right]^{\frac{1}{2}}$.

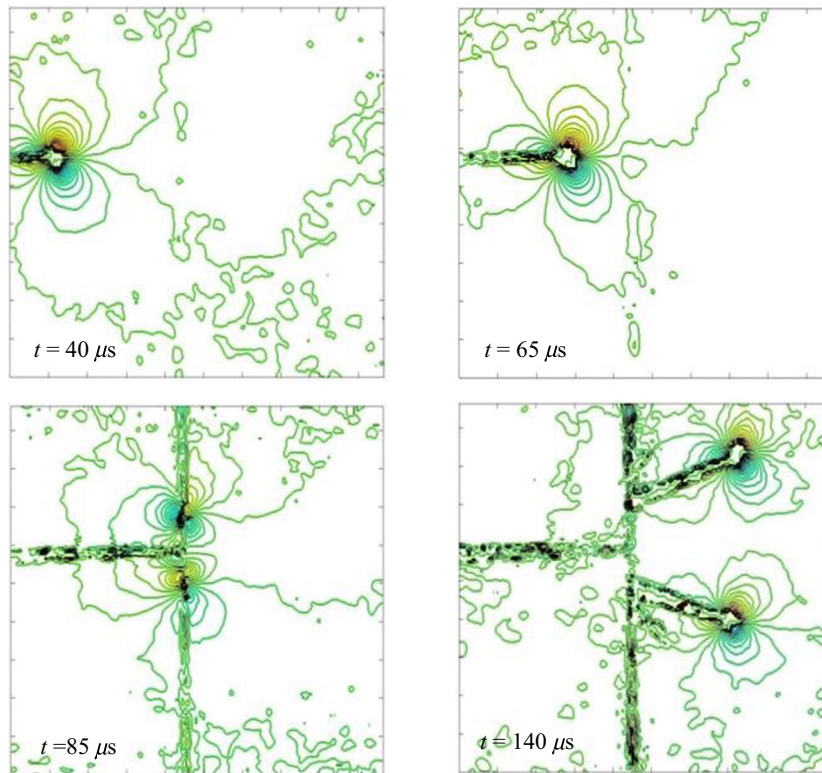
In the above equations, C is the crack-tip velocity, C_L and C_S are longitudinal and shear wave speeds respectively, ρ is the mass density, μ and ν are shear modulus and Poisson's ratio respectively. Further, note that Equations (14)–(17) reduce to the form of a dynamically loaded stationary crack in the limit $C \rightarrow 0$.

To evaluate SIF histories, the angular deflection fields were digitized by identifying the current crack-tip location and crack direction. Subsequently the local Cartesian and polar

Fig. 15 Angular deflection contour plots (contour interval = 8×10^{-4} rad) proportional to stress-gradients in the x - and y -directions for a bi-layered specimen with 'weak' interface



(a) ϕ_x Contours



(b) ϕ_y Contours

coordinates were established. A number of discrete data points (orthogonal angular deflection values) around the crack-tip in the region $0.25 \leq r/B \leq 0.75$ and an angular extent $-135^\circ \leq \theta \leq 135^\circ$ were collected and stored. This ensured that data close to the crack-tip where triaxial effects are dominant and the data near the crack faces influenced by edge effects are largely excluded from the analysis [18]. At each data point the angular deflection components in global coordinate system as well as their location were stored. These digitized data along with the angle of rotation of the crack at that time instant were used in Equation (14) for $N \leq 4$ to perform an over-deterministic least-squares analysis to estimate both mode-I and mode-II SIFs. This process was repeated for all 32 pairs of images and for each time step to generate SIF histories. Since the crack growth occurred in mixed-mode conditions, the SIFs were used to evaluate strain energy release rate, G , and mode-mixity, ψ , as [30],

$$G(t) = \frac{K_I^2(t) + K_{II}^2(t)}{E}; \psi(t) = \tan^{-1} \left(\frac{K_{II}(t)}{K_I(t)} \right) \quad (18)$$

where E is the elastic modulus.

Experimental Results

Crack Path Selection and Angular Deformation Histories

Photographs of three fractured samples from each configuration representing monolithic and two layered specimens with ‘weak’ and ‘strong’ interfaces are shown in Fig. 13. The impact point is located on the left edge along the V-notched faces of each image and crack propagation direction is from the left to right as shown by the arrowhead. In each case it is evident that the crack propagated self-similarly under mode-I conditions until it reached the interface vicinity. Differences in crack paths occurred subsequently for layered configurations whereas for the monolithic specimen, the crack continued to grow in a self-similar path until it reached the final third of the uncracked ligament beyond which it deviated from its initial path due to a loss of in-plane constraint [31] as it approached the free edge. Figure 13(a) shows the crack path for a monolithic specimen. Figure 13(b) and (c) show crack paths for a weak and strong interface, respectively. In these, more complex fracture patterns involving interfacial crack growth and mixed-mode crack branching in layer-II are evident. Thus, the interface caused a single mode-I crack in layer-I to branch into two nearly symmetric interface cracks before emerging as two mixed-mode daughter cracks in layer-II. This clearly shows that the introduction of the interface greatly perturbs crack growth causing the crack to branch and create greater surface

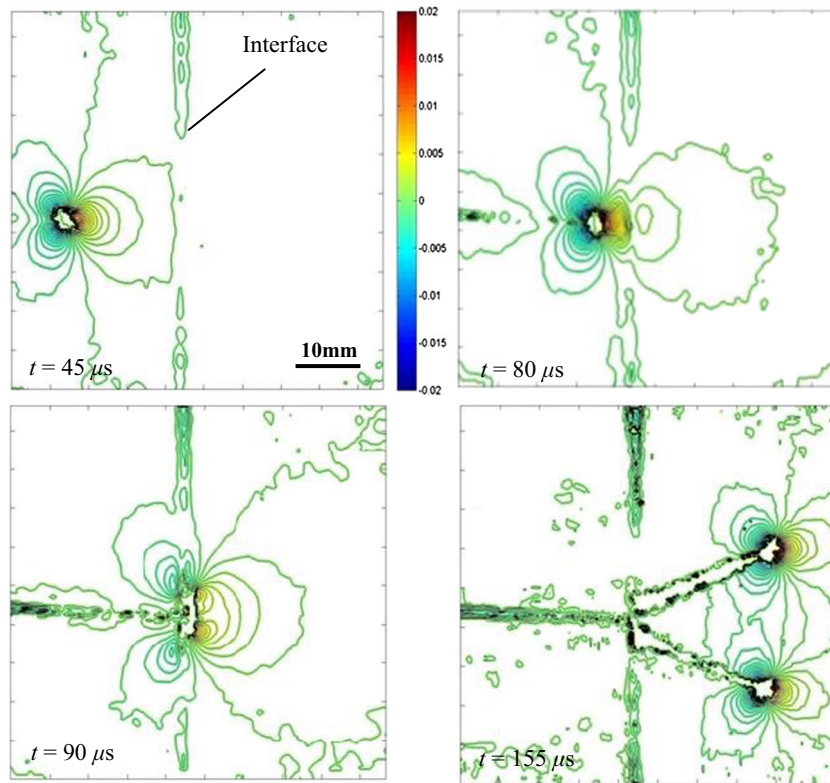
area. In the specimen with a weak interface, the trapped interface cracks traveled for a longer distance (~ 12 mm) along the interface when compared to the specimen with a strong interface (~ 4 mm). Further, the angle of emergence of the two daughter cracks in layer-II is higher in case of the strong interface ($\sim 28^\circ$) when compared to the weak counterpart ($\sim 18^\circ$) as the crack emerged into layer-II. Despite the intrinsic complexities, these experiments were quite repeatable as detailed in Appendix 2.

Plots of angular deflection contours derived from the image correlation data are shown in Figs. 14, 15, and 16. Note that plots presented here are only for four select time instants for the sake of brevity. (The angular deflection contours, the contour levels and the scale bar are shown in the first plot in each set and are applicable to the other plots as well.) In these $t = 0 \mu\text{s}$ represents the time at which the crack initiated at the original sharpened notch tip. In each figure, sets (a) and (b) correspond to ϕ_x and ϕ_y contours, respectively.

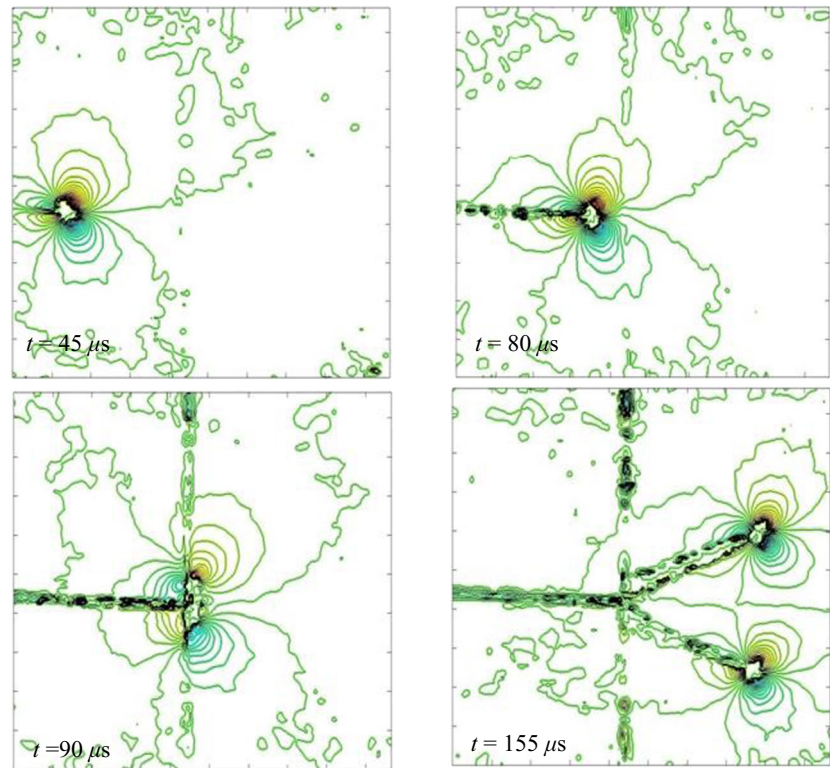
Figure 14 shows angular deflection contours for a monolithic specimen. The crack followed a nearly straight path during the time window of interest suggesting a predominantly mode-I behavior. The overall size of contours remained approximately unchanged during crack growth suggesting a constant stress intensity factors in the window of observation. It should also be noted that ϕ_x contours are symmetric in shape and magnitude with respect to the growing crack whereas ϕ_y contours are only symmetric in shape but antisymmetric in magnitude. Figure 15 shows angular deflection contours in a layered material with a weak interface. Initially the crack travels self-similarly in layer-I as in the monolithic specimen. When it approaches the interface, a distortion in the lobes ahead of the crack-tip for ϕ_x contours is evident while no significant distortion is observed in the corresponding ϕ_y contours. Later it can be seen that the interface causes the crack to branch into two symmetric (with respect to the x -direction) daughter cracks propagating along the interface in mixed-mode condition as evident from asymmetric (relative to crack growth direction) tri-lobed structures typical of crack-tip stress gradient fields [16, 32]. Subsequently two daughter cracks emerge from the interface into layer-II and propagate nearly symmetrically, again under mixed-mode condition. Interaction between these two daughter cracks can also be observed as some of the contours of the upper branch are linked with those of the lower branch.

The same distinct features at various time instants can be observed in the angular deflection contours for the specimen with a strong interface in Fig. 16. Major differences here include the extent of crack growth along the interface and angle of emergence of the two daughter cracks into layer-II.

Fig. 16 Angular deflection contour plots (contour interval = 4×10^{-4} rad) proportional to stress-gradients in the x - and y -directions for a bi-layered specimen with ‘strong’ interface



(a) ϕ_x Contours



(b) ϕ_y Contours

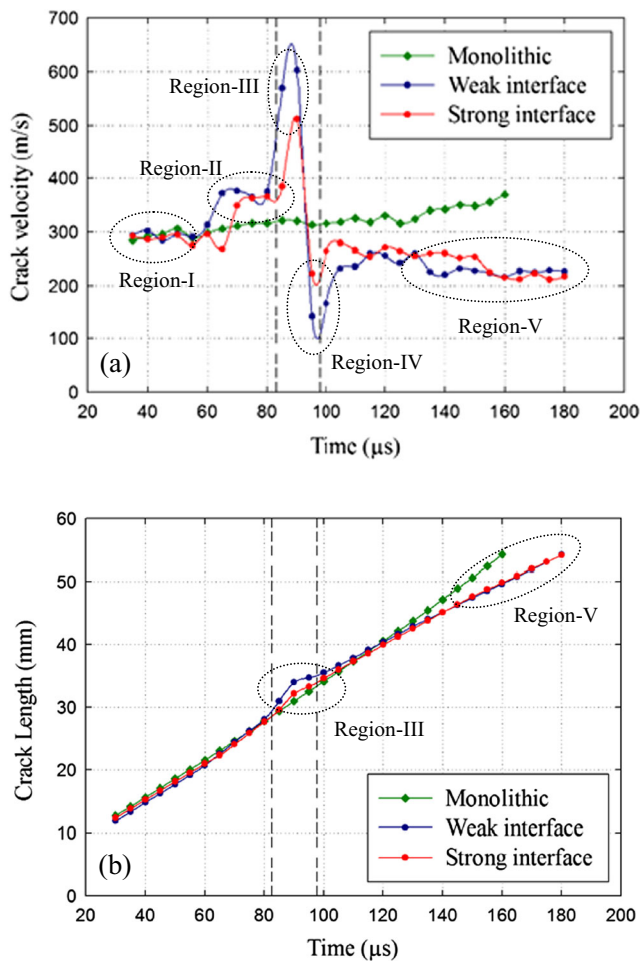


Fig. 17 Crack growth histories: (a) Crack velocity histories and (b) Crack length histories, for specimens with ‘strong’ and ‘weak’ interfaces and a monolithic specimen. The region between the vertical broken lines qualitatively represents the interface vicinity

Crack Growth Histories

Figure 17(a) and (b) show the plots of crack velocity and length histories, respectively, for all the three configurations. It should be noted that $t=0 \mu\text{s}$ represents the time at which the crack initiates at the original notch tip. Five distinct regions in the velocity histories can be seen for bi-layered specimens relative to the monolithic counterpart. A pair of vertical broken lines is used to qualitatively demarcate the time instants at which the crack-tip is in the interface vicinity. In region-I, following crack initiation, a constant crack velocity trend for propagation in layer-I under mode-I conditions can be seen. The crack velocities of specimens with interfaces are similar to that of the monolithic specimen in this region. In region-II, a step increase in crack velocity for the two bi-layered cases is observed as the crack-tip approaches the interface. This suggests an increase in crack-tip driving force as stress waves

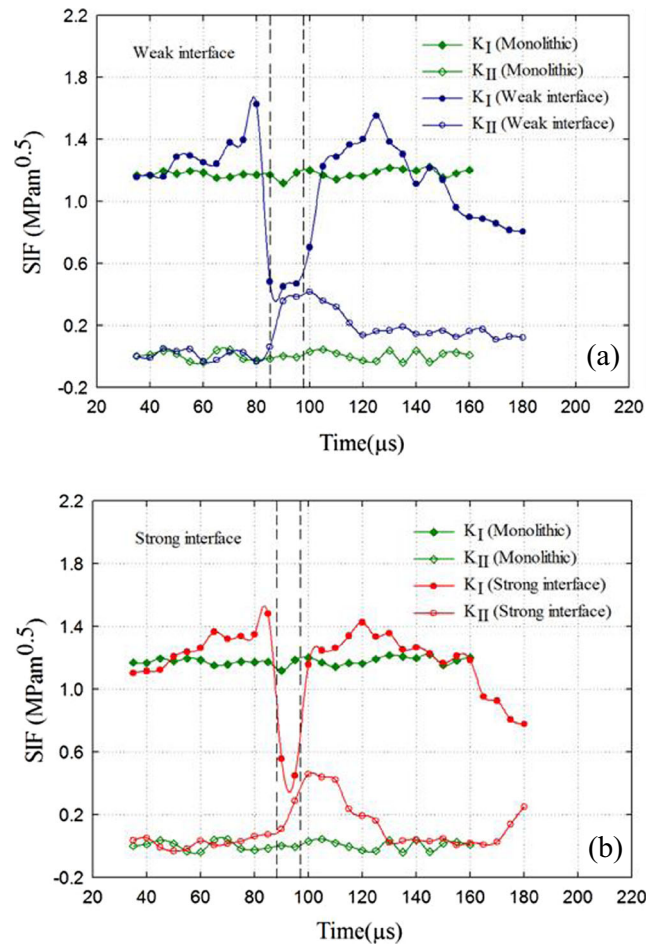


Fig. 18 Stress intensity factor (SIF) histories for a bi-layered specimen with (a) weak interface and (b) strong interface and their comparison with those for a monolithic counterpart

reflect off the interface, communicating to the crack tip the presence of a region of weakness (relative to the monolithic material) ahead. In region-III, a rapid increase in crack velocity (and crack length) is observed as the crack propagates along the interface in the form of *two* trapped interfacial crack-tips. The computed crack velocity in case of a specimen with a weak interface is generally higher when compared to the strong counterpart. This is in agreement with the higher travel distance for the crack along the interface in case of a specimen with the weak interface as compared to the strong interface. In region-IV a rapid deceleration of the two daughter cracks² can be seen as the crack is about to exit the interface and penetrate layer-II. This is because of the resistance offered by layer-II for the crack propagation as compared to the interface as well as formation of two daughter cracks resulting in

² Note that data for only one of the two cracks is shown in Fig. 17.

greater crack surface area. It can be seen that for a specimen with a weak interface, the dip in crack velocity is greater when compared to the one with a strong interface, which is to be expected. Region-V shows crack velocities (and crack length) in layer-II for bi-layered specimens to be much lower relative to the monolithic counterpart.

SIF, Strain Energy Release Rate and Mode-Mixity Histories

The stress intensity factor histories for all the configurations evaluated from the angular deflection fields and the least-squares analysis discussed earlier is plotted in Fig. 18. The set of vertical broken lines qualitatively suggests the interface ‘vicinity.’ Figure 18(a) shows SIF histories of a specimen with a weak interface relative to a monolithic specimen. It can be seen that K_I for a monolithic specimen is nearly constant and K_{II} is oscillatory about zero for the duration of crack growth in the observation window. This behavior is to be expected since crack growth occurred in the monolithic case predominantly

under mode-I condition. (It should be noted that oscillations seen in the K_{II} values about zero suggests the accuracy of the least-squares analysis undertaken in this work.) Initially, K_I for the specimen with a weak interface is same as that for the monolithic case but as the crack approaches the interface, K_I increases gradually to a peak value of $1.62 \text{ MPa}\sqrt{\text{m}}$ whereas K_{II} remains nearly zero until it reaches the interface. Further, as the crack enters the interface, K_I drops while K_{II} increases rapidly suggesting a significant increase in the shear component and hence mode-mixity as the trapped cracks propagates along the interface. When cracks penetrate layer-II, K_I increases to values above that in the monolithic configuration before decreasing gradually whereas K_{II} attains it peak value of $0.41 \text{ MPa}\sqrt{\text{m}}$ just as it emerges from the interface before dropping off precipitously. (It is worth noting that the values of K_I and K_{II} in the interface and layer-II are shown for only one crack-tip (upper branch) in these plots and in reality there are two daughter cracks to consider.) It can be seen that the final K_I for the specimen with a weak interface is much lower than that of the monolithic case whereas K_{II} is marginally

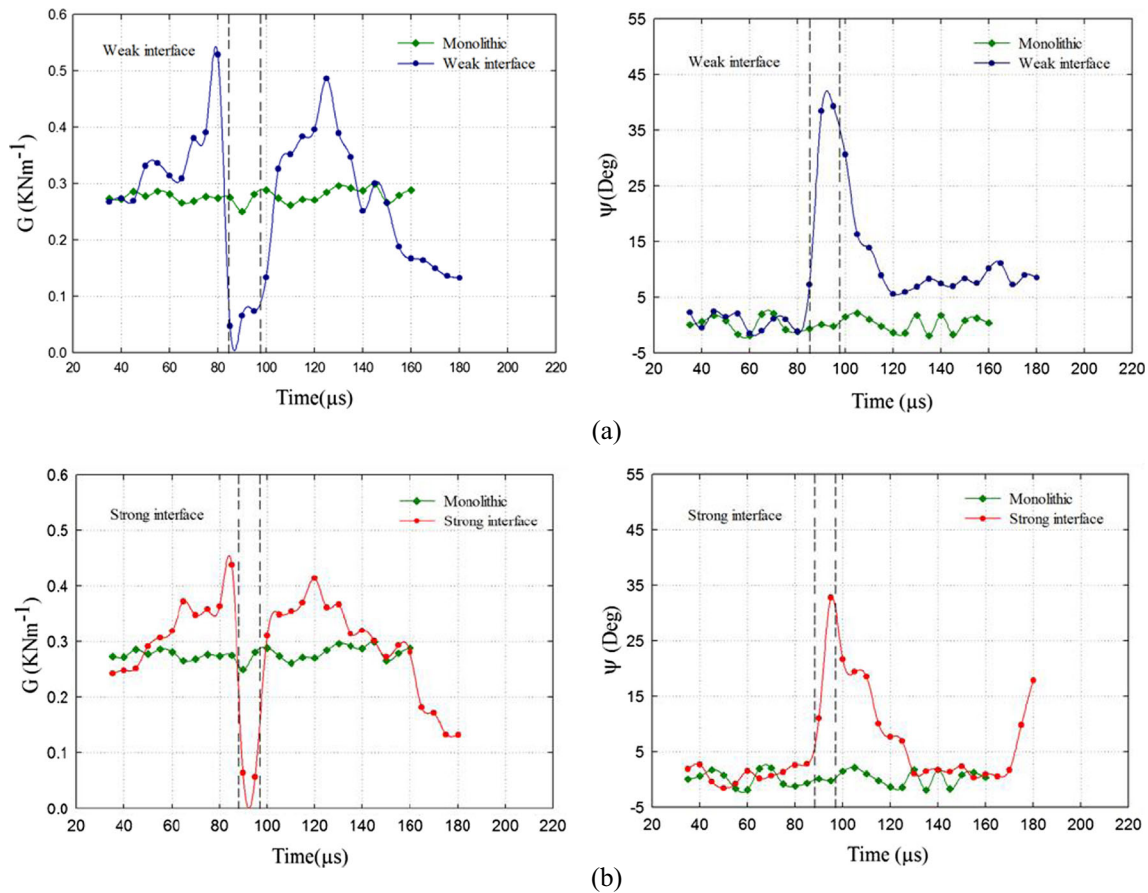


Fig. 19 Strain energy release rate (G) and mode-mixity (ψ) histories for a bi-layered specimen with (a) weak interface and (b) strong interface and their comparison with those of a monolithic counterpart

higher suggesting a reduction in the final crack driving force. Figure 18(b) shows the SIF histories of a specimen with a strong interface relative to the monolithic counterpart. The sample with a strong interface also shows similar distinct characteristics; a peak K_I value of 1.51 MPa $\sqrt{\text{m}}$ and a peak K_{II} of 0.49 MPa $\sqrt{\text{m}}$. Final K_I values towards the end of the observation window (with a substantially lower K_{II}) for bi-layered specimens are much lower relative to the monolithic case demonstrating that the introduction of an interface reduces the stress intensity factors significantly as more energy is expended in the formation of two daughter cracks and new surfaces. It can also be seen that, throughout the crack propagation, K_I and K_{II} for the specimen with a weak interface is higher than the specimen with a strong interface suggesting that more energy was dissipated in the former.

The strain energy release rate (G) and mode-mixity (ψ) histories evaluated using K_I and K_{II} data are shown in Fig. 19. Similar to the earlier discussion on SIFs, the same distinct features can be seen in the G histories. The final G for specimens with an interface (both strong and weak cases) is much lower ($\sim 130 \text{ Nm}^{-1}$) than that of the monolithic counterpart ($\sim 280 \text{ Nm}^{-1}$), shown in Fig. 19(a) and (b) (left), which is about 54 % reduction without altering the weight to the structure. (As noted earlier, the values of G in case of bi-layered specimens, along the interface and in layer-II, are shown only for one crack-tip, the upper branch in these plots, and in reality there are two daughter cracks to consider.) Referring to the mode-mixity plots, the specimen with a weak interface compared to the monolithic specimen, shown in Fig. 19(a) (right), an oscillatory mode-mixity about zero can be seen until the crack reaches the interface vicinity. As the crack enters the interface, the mode-mixity increases rapidly to a maximum value of $\sim 39^\circ$. Subsequently, as the crack emerges from the interface the mode-mixity decrease gradually to $\sim 8^\circ$. In case of a specimen with a strong interface, shown in Fig. 19(b) (right), similar features can be seen as well. The peak mode-mixity of $\sim 33^\circ$ is observed when the crack travels along the interface. Further, as the crack penetrates layer-II, the mode-mixity gradually falls and as it travels further in layer-II, the mode-mixity approaches zero. (Towards the end of observation window, the mode-mixity increases, possibly a local aberration.) It is observed that the mode-mixity during crack penetration into layer-II is higher ($\sim 21^\circ$) in case of specimen with a strong interface when compared to that with a weak interface ($\sim 16^\circ$). This is consistent with the earlier observation of higher angle of penetration into layer-II for the strong interface case when compared to its weak counterpart.

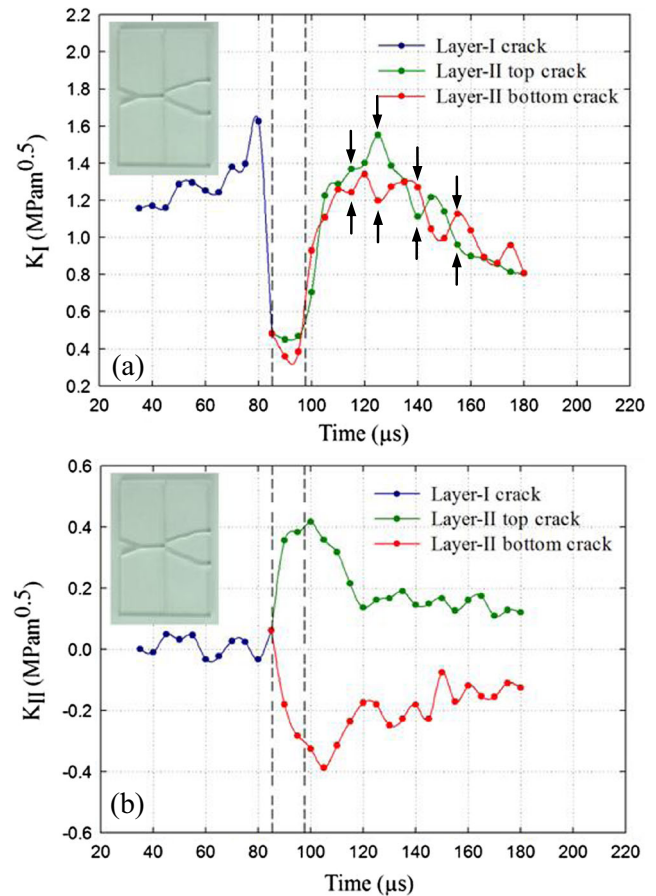


Fig. 20 Interaction between branched cracks: (a) Mode-I, and (b) mode-II SIF histories for the two daughter cracks in layer-II for bi-layered specimen with a weak interface. Out-of-phase oscillations in K_I values for the two daughter cracks are evident during propagation in layer-II

Interaction Between Daughter Cracks

As observed in the earlier sections, there are two successful daughter cracks in layer-II for both types of bi-layered specimens. Also, in all the earlier plots, the SIF histories for one of the daughter cracks (top branch) were presented. In this section, SIF histories for both the top and the bottom cracks are discussed. Figure 20(a) and (b) show K_I and K_{II} histories, respectively, for both the daughter cracks. The crack-tip fields show interaction with each other as noted earlier (Figs. 15 and 16) and the resulting intertwined pattern of K_I histories is evident in Fig. 20(a). Interestingly, K_I of the top crack is higher than that for the bottom crack at an instant whereas the values reverse in the next. This behavior can be observed rather consistently throughout the observation window in layer-II and are highlighted by a pair of opposing arrows in Fig. 20(a) at a few time instants. That is, when one crack-tip is

experiencing a high value, the other is at a low value. At the same time instants, the K_{II} values (Fig. 20(b)) for the two daughter cracks are comparable in magnitudes but are opposite in sign. That is, the upper crack is experiencing a positive shear and a positive K_{II} whereas the lower is experiencing a negative shear and a negative K_{II} .

Discussion

Similar to the previous studies [7, 12, 13], in a homogenous monolithic specimen the crack propagated dynamically under mode-I condition whereas in bi-layered configurations with an interface the crack propagated in mixed-mode along the interface and in the subsequent layer even when loaded symmetrically in the far field. In case of mixed-mode crack propagation, the DGS contours show similarities with the mixed-mode CGS contours reported in a few previous works [17, 19]. Further, the availability of two orthogonal stress gradient fields in DGS offered additional ways of extracting fracture parameters relative to the ones previously demonstrated [19]. During crack propagation along the interface, there was a dramatic jump in crack speed [7, 12]. Further, higher crack speeds along the interface were observed in case of the weak interface with values comparable to a few previous reports [7, 12, 17]. Further, as in the earlier studies [7, 12, 13, 14], there were crack penetration into layer-II. Unlike the previous studies, a combination of crack branching and penetration mechanisms was observed at an interface. The crack initially deflected into and subsequently branched off the interface before penetrating layer-II. The two daughter cracks in layer-II propagated symmetrically relative to the initial crack path in layer-I, not observed previously. There was a significant reduction in crack velocity in the layer-II with the introduction of an interface, largely attributed to crack penetration and mixed-mode propagation in layer-II. Further, the results provide both qualitative and quantitative evidence that the two propagating daughter cracks continuously interact with each other as they grow in layer-II resulting with an out-of-phase (pulsating) variation of K_I for the two crack tips. The physical significance of this, if any, is yet to be understood. Further, a significant reduction in strain energy release rate caused by the introduction of the interface was observed. That is, layering of the material enhanced the fracture energy dissipation in otherwise homogeneous material. The results also suggest the possibility of enhancing fracture energy absorption by tailoring interfacial fracture toughness without altering the weight to the structure. Other possibilities such as increasing the number of interfaces, grading interface strengths sequentially and tailoring individual layer thicknesses need further investigation.

Conclusions

DGS is a powerful full-field optical method useful for studying fracture and failure mechanics of monolithic and layered materials. In this work it is successfully extended to visualize and quantify dynamic crack initiation and growth characteristics of monolithic and layered PMMA sheets. An approach for evaluating SIFs of mixed-mode cracks using DGS technique is outlined. The approach is successfully extended to examine dynamic fracture mechanics of layered architectures. Unlike a monolithic specimen, crack branching and mixed-mode crack propagation occur in layered counterparts. The SIF histories as well as crack velocity histories for growing cracks entering and exiting an interface as well as when trapped in the interfaces show significant gyrations. Final crack velocities/crack lengths observed in specimens with interface suggests that interfaces can effectively obstruct and perturb crack propagation in otherwise homogeneous materials. The energy release rate at branched crack-tips in both strong and weak interface cases is lower than their monolithic counterpart at advanced stages of crack growth. Further, higher mode-mixity and strain energy release rate throughout the fracture event in the specimen with a weak interface (relative to the strong interface) shows that it is a more favorable configuration. More importantly, the weight of the layered configurations is nominally identical to the monolithic counterpart.

Acknowledgments The support for this research by the U.S. Army Research Office through grant W911NF-12-1-0317 is gratefully acknowledged.

Appendix 1

Mixed-Mode FE Simulation

A complementary quasi-static finite element simulation of the mixed-mode tension experiment was carried out using ABAQUS® software. The model was discretized into 4589 four node bilinear plane stress quadrilateral elements. The local seeding around the crack-tip was used to generate a fine mesh in the crack-tip vicinity. Table 1 shows the material properties of PMMA used in the simulation. The discretized model and the boundary conditions used are shown in Fig. 21. Displacements corresponding to the cross-head speed during the experiment were imposed at one end of the specimen in a series of steps. A local coordinate system aligned with the crack direction was defined for post-processing the data. The crack opening (COD) and crack sliding (CSD) displacements were extracted along the two crack faces. This was repeated for each displacement step. The apparent mode-I and mode-II

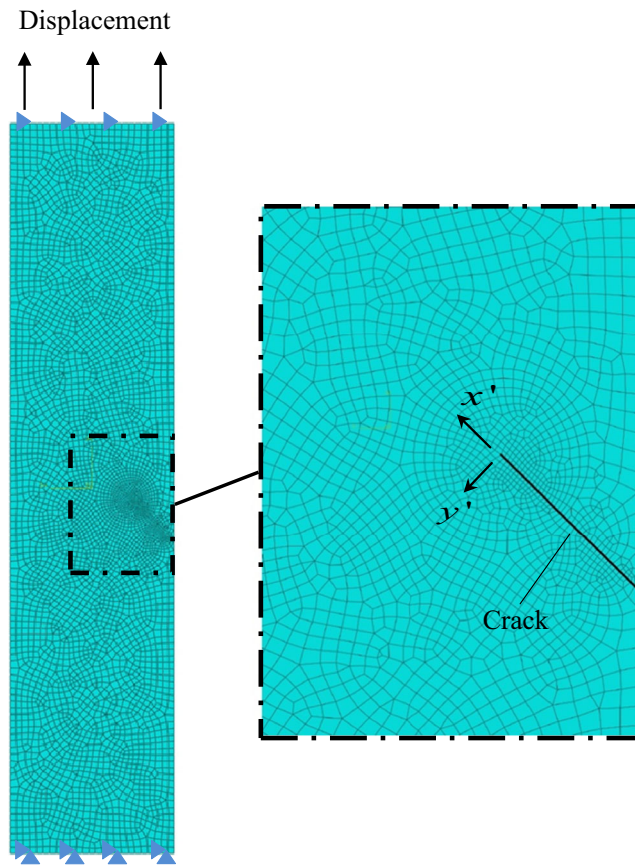


Fig. 21 Details of the numerical simulations; finite element model showing the discretization and the boundary conditions used

SIFs, $(K_I)_{app}$ and $(K_{II})_{app}$ at each displacement step were computed using [26],

$$(K_I)_{app} = \frac{E\sqrt{2\pi}}{4\sqrt{r}}u_{y'}; (r, \theta = \pi) \quad (19)$$

$$(K_{II})_{app} = \frac{E\sqrt{2\pi}}{4\sqrt{r}}u_{x'}; (r, \theta = \pi) \quad (20)$$

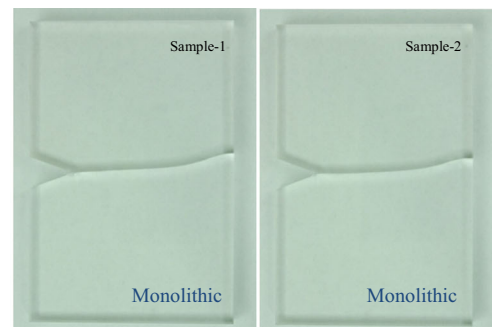
where E is the elastic modulus, (r, θ) are the crack-tip polar coordinates, $u_{y'}$ is the half COD and $u_{x'}$ is the half CSD of the crack flanks. By extrapolating the linear portion of $(K_I)_{app}$ and $(K_{II})_{app}$ values plotted as a function of the radial distance r to the crack tip, the true K_I and K_{II} were determined.

Appendix 2

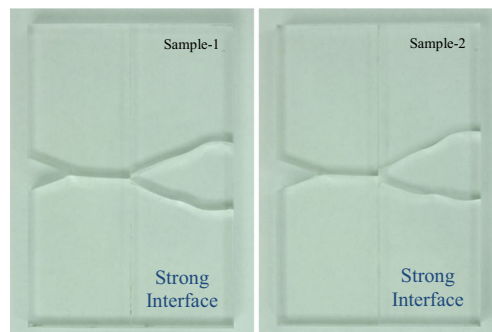
Experimental Repeatability

Multiple experiments were conducted for monolithic and bi-layered configurations (both weak and strong interface cases) to ensure repeatability in terms of dynamic fracture behavior as well as fracture parameters. Fig. 22(a) shows photographs of two fractured samples of monolithic specimen whereas

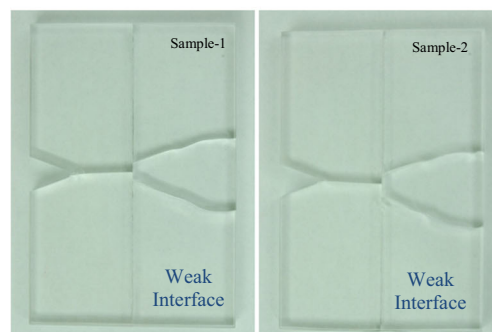
Fig. 22(b) and (c) show two fractured samples of specimens with strong and weak interface, respectively. A high degree of reproducibility in crack paths throughout the fracture event (well past the interface) is clearly evident in Figs. 22(b) and (c). Figure 23(a) and (b) show SIF histories for two different samples with a weak and a strong interface, respectively. Again, repeatability can be readily seen in the measured values of SIF histories too. That is, the SIF histories of multiple samples closely agree with each other before the crack reaches the interface. After the crack penetrates the second layer there are only marginal differences between the two SIF histories. Despite the highly transient nature of the problem, and the possibility of potential variations in material and interface characteristics, a rather high degree of reproducibility is evident.



(a) Monolithic specimens.



(b) Specimens with strong interface.



(c) Specimens with weak interface.

Fig. 22 Multiple fractured samples of each configuration

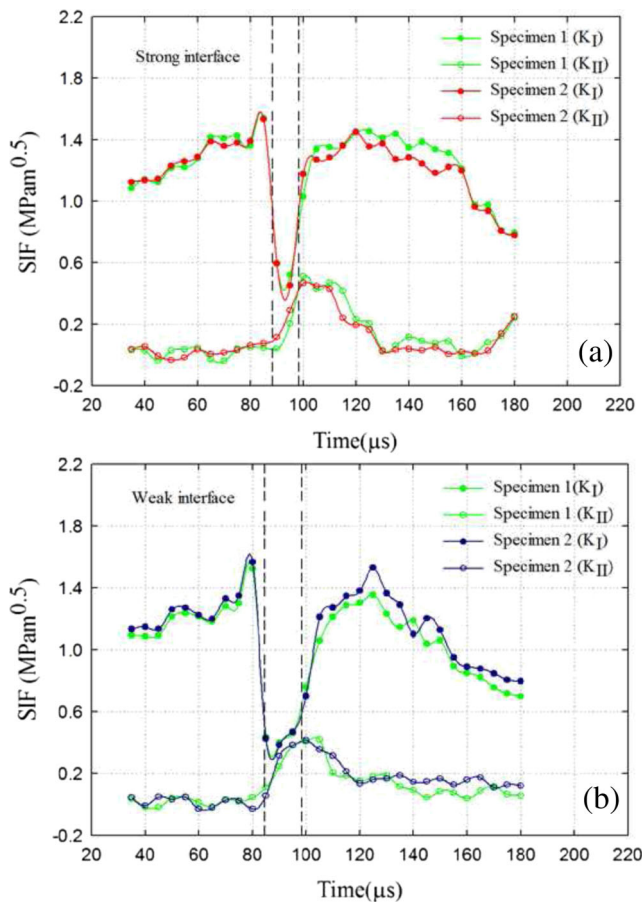


Fig. 23 SIF histories for multiple fractured samples of each configuration. The vertical broken lines denote the crack tip vicinity

References

- Patel PJ, Gilde GA, Dehmer PG, McCauley JW (2000) Transparent armor. AMPTIAC Newslett 4(3)
- Subhash G (Guest Editor) (2013) Special issue on 'Transparent Armor Materials'. Exp Mech 53(1):1–2
- Wang J, Xu Y, Zhang W (2014) Finite element simulation of PMMA aircraft windshield against bird strike by using a rate and temperature dependent nonlinear viscoelastic constitutive model. Compos Struct 108:21–30
- Raghuvanshi RK, Verma VK (2014) Mechanical and thermal characterization of aero grade polymethyl methacrylate polymer used in aircraft canopy. Int J Eng Adv Tech (IJEAT) 3(5):216–219
- Freund LB (1990) Dynamic fracture mechanics. Cambridge University Press, New York
- Broberg KB (1999) Cracks and fracture. Academic, San Diego
- Xu LR, Huang YY, Rosakis AJ (2003) Dynamic crack deflection and penetration at interfaces in homogeneous materials: experimental studies and model predictions. J Mech Phys Solids 51:461–486
- Washabaugh PG, Knauss WG (1994) A reconciliation of dynamic crack growth velocity and Rayleigh wave speed in isotropic brittle solids. Int J Fract 65:97–114
- Rosakis AJ, Samudrala O, Coker D (1999) Cracks faster than shear wave speed. Science 284:1337–1340
- Hutchinson JW, Suo Z (1992) Advances in applied mechanics, vol. 29. Academic, New York, pp 63–191
- Suresh S, Sugimura Y, Tschegg EK (1992) Growth and fatigue crack approaching a perpendicular-oriented bimaterial interface. Scr Metall Mater 27:1189–1194
- Chalivendra VB, Rosakis AJ (2008) Interaction of dynamic mode-I cracks with inclined interfaces. Eng Fract Mech 75:2385–2397
- Park H, Chen W (2011) Experimental investigation on dynamic crack propagating perpendicular through interface in glass. J Appl Mech 78(5):051013
- Xu LR, Rosakis AJ (2003) An experimental study of impact-induced failure events in homogeneous layered materials using dynamic photoelasticity and high-speed photography. Opt Lasers Eng 40:263–288
- Xu LR, Rosakis AJ (2005) Impact damage visualization of heterogeneous two-layer materials subjected to low-speed impact. Int J Damage Mech 14:215–233
- Mason JJ, Lambros J, Rosakis AJ (1992) The use of a coherent gradient sensor in dynamic mixed-mode fracture mechanics experiments. J Mech Phys Solids 40(3):641–661
- Tippur HV, Rosakis AJ (1991) Quasi-static and dynamic crack growth along bimaterial interfaces: A note on crack-tip field measurements using coherent gradient sensing. Exp Mech 31(3):243–251.
- Tippur HV, Krishnaswamy S, Rosakis AJ (1992) Optical mapping of crack-tip deformations using the methods of transmission and reflection coherent gradient sensing: A study of crack-tip K -dominance. J Mech Phys Solids 40(2):339–372
- Kirugulige MS, Tippur HV (2006) Mixed-mode dynamic crack growth in functionally graded glass-filled epoxy. Exp Mech 46(2):9–281
- Singh RP, Lambros J, Shukla A, Rosakis AJ (1997) Investigation of the mechanics of intersonic crack propagation along a bimaterial interface using coherent gradient sensing and photoelasticity. Proc R Soc Lond A 453:2649–2667
- Winkler S, Shockey DA, Curran DR (1970) Crack propagation at supersonic velocities I. Int J Fract Mech 6:151–158
- Curran DR, Shockey DA, Winkler S (1970) Crack propagation at supersonic velocities II. Theoretical model. Int J Fract Mech 6:271–278
- Periasamy C, Tippur HV (2012) A full-field digital gradient sensing method for evaluating stress gradients in transparent solids. Appl Opt 51(12):2088–2097
- Periasamy C, Tippur HV (2013) Measurement of orthogonal stress gradients due to impact load on a transparent sheet using digital gradient sensing method. Exp Mech 53:97–111
- Williams ML (1959) On the stress distribution at the base of a stationary crack. J Appl Mech 24:109–114
- Periasamy C, Tippur HV (2013) Measurement of crack-tip and punch-tip transient deformations and stress intensity factors using digital gradient sensing technique. Eng Fract Mech 98:185–199
- Xu LR, Rosakis AJ (2003) Real-time experimental investigation of dynamic crack branching using high-speed optical diagnostics. Exp Tech 23–26
- Freund LB, Rosakis AJ (1992) The structure of the near-tip field during transient elastodynamic crack growth. J Mech Phys Solids 40:699–719
- Chalivendra V, Shukla A (2005) Transient elastodynamic crack growth in functionally graded materials. J Appl Mech 71:237–248
- Kitey R, Tippur HV (2008) Dynamic crack growth past stiff inclusion: Optical investigation of inclusion eccentricity and inclusion-matrix adhesion strength. Exp Mech 48(1):37–54
- Maleski MJ, Kirugulige MS, Tippur HV (2004) A method for measuring mode I crack tip constraint under static and dynamic loading conditions. Exp Mech 44(5):522–532
- Mello M, Hong S, Rosakis AJ (2009) Extension of the coherent gradient sensor (CGS) to the combined measurement of in-plane and out-of-plane displacement field gradients. Exp Mech Special edition 49:277–289